CHALMERS

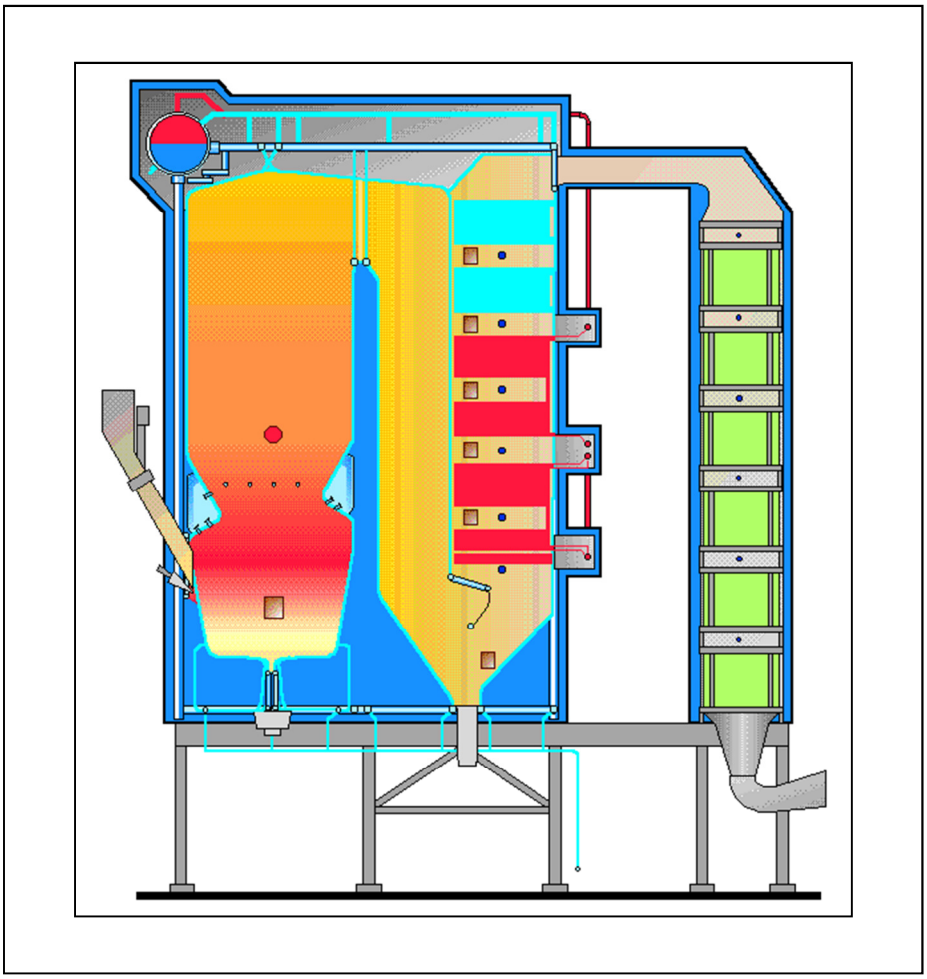

Modelling Heat Transfer in the Cooling Pass of a Refuse-Fired Fluidised Bed Combustor

Master of Science Thesis in the
Master's Degree Programme, Sustainable Energy Systems

LOUISE AXELSSON

Chalmers University of Technology
Department of Energy and Environment
Division of Energy Technology
Report No. T2012-381

Göteborg, Sweden 2012
Report No. T2012-381

REPORT NO. T2012-381

Modelling Heat Transfer in the Cooling Pass of a Refuse-Fired Fluidised Bed Combustor

LOUISE K.C. AXELSSON

Department of Energy and Environment
CHALMERS UNIVERSITY OF TECHNOLOGY
Gothenburg, Sweden 2012

Modelling Heat Transfer in the Cooling Pass of a Refuse-Fired Fluidised Bed Combustor
LOUISE K.C. AXELSSON

Technical Report No. T2012-381
Department of Energy and Environment
Chalmers University of Technology
SE-412 96 Göteborg
Sweden
Telephone + 46 (0)31-772 1000

Cover: Energy from Waste boiler, with permission from Jan Olofsson, Metso Power AB.
Reproservice
Göteborg, Sweden 2012

Preface

This master's thesis has been carried out within the master's programme Sustainable Energy Systems at the Department of Energy and Environment at Chalmers University of Technology. The master's programme includes several courses that focus on energy optimisation and heat transfer, as well as environmental issues. Some areas that are covered are gas and steam turbines, power boilers, heat pumps, heat exchangers and pinch analysis, with a focus on optimisation and design. The elective courses that were chosen covered areas such as CFD, multiphase flows and combustion engineering.

The master's thesis was a collaboration between Chalmers, Epsilon AB and Metso Power AB. Metso Power AB's goal is to increase the efficiency of their Energy from Waste boilers by introducing a superheater in the cooling pass before the convective zone. The thesis consisted of the creation of a 1D model that calculates the steam and flue gas temperatures leaving the flue gas cooling pass. Correlations from the literature and CFD simulations were used in the creation of this model.

The author would like to thank Christian Johansson and Christoffer Källerman at Epsilon AB, Jan Olofsson at Metso Power AB and David Pallarès at Chalmers for their guidance and time.

Nomenclature

Roman uppercase letters
A = area [m^2]
C = anisotropy of scattering [-]
C_v = volumetric fraction of dust particles [-]
C_p = heat capacity [J/kg/K]
D = diameter [m]
E = total energy [m^2/s^2]
E_p = equivalent emission [W/sr/m]
F = view factor [-]
$\vec{F}$ = external body forces [N/m^2]
G = incident radiation [W/m^2]
I = radiation intensity (depends on position $\vec{r}$ and direction $\vec{s}$) [W/sr]
I_0 = radiation intensity at the wall [W/sr]
I_λ = spectral intensity [W/sr/m]
$I_{b\lambda}$ = black body intensity [W/sr/m]
J_j = diffusion flux of species j [$kg/m/s^3$]
K = Friction loss factor [-]
L = characteristic length [m]
L = tube length [-]
N = number of wavelength bands [-]
ΔP = pressure loss [Pa]
S_m = mass source term [$kg/m^3/s$]
S_h = energy source term [kg/s^3m]
T = temperature [K]
U = overall heat transfer coefficient [$W/m^2/K$]
V = volume [m^3]
X = volume fraction [-]

Roman lowercase letters
a = absorption coefficient [m^{-1}]
a_p = equivalent absorption coefficient due to presence of particles [m^{-1}]
a_λ = spectral absorption coefficient [m^{-1}]
d = depth of cooling pass [m]
ds = particle size [m]
f_f = friction factor [-]
f_k = correction factor for the flue gas emissivity [-]
g = gravitational acceleration [m/s^2]
h = height of the cooling pass [m]
h = convective heat transfer coefficient [$W/m^2/K$]
h_j = sensible enthalpy of species j [J/kg]
k_{eff} = effective conductivity [W/m/K]
l = thickness used for calculating the conductive heat transfer [m]
$\dot{m}$ = mass flow rate [kg/s]
n = refractive index [-]
n = number of steps [-]
$\vec{n}$ = normal vector [-]
n_t = number of tubes [-]
p = pressure [Pa]

$\vec{r}$ = position vector [-]
s = path length [m]
s = mean beam length [m]
$\vec{s}$ = direction vector [-]
$\vec{s}'$ = scattering direction vector [-]
t = time [s]
v = velocity [m/s]
q = radiative heat flux [W]
q_{in} = incident radiative heat flux [W]
q_{out} = outgoing radiative heat flux [W]
Δx = size of one discrete cell [m]
w = width of the cooling pass [m]

Greek letters
α = absorptivity [-]
δ = tolerance [-]
ε = emissivity [-]
$\Delta\lambda$ = wavelength band [m]
λ = wavelength [m]
λ = thermal conduvtivity [W/m/K]
μ = viscosity [Pas]
ρ = density [kg/m^3]
σ = Stefan-Boltzmann constant (5.672×10^{-8} W/m^2/K^4)
σ_p = equivalent particle scattering coefficient [m^{-1}]
σ_s = scattering coefficient [m^{-1}]
$\overline{\tau}$ = stress tensor [N/m^2]
$\bar{\bar{\tau}}_{eff}$ = effective stress tensor [N/m^2]
φ = fraction of energy absorbed by the flue gas [-]
Φ = phase function [-]
Ω' = solid angle [sr]

Indices
1 = first cell of the cooling pass
CO_2 = carbon dioxide
cr = crossectional
D = diameter, characteristic length
fg = flue gas
g = gas
gg = gas-gas
gi = gas-surface i
gy = gas-surface y
gz = gas-surface z
H_2O = water vapour
i = inner tube of steampipe
i = surface i
in = ingoing
inner = inner diameter
is = inner steam: “colder” steam in inner tubes flowing in positive x-direction
j = surface j
ji = j to i

L = hydraulic diameter, characteristic length
left = left side of the superheater according to. 2.3
m = arbitrary cell in cooling pass
n = arbitrary cell in cooling pass
N = last cell of cooling pass
N_2 = nitrogen
O_2 = oxygen
o = outer tube of steampipe
os = outer steam: “hotter” steam in outer tubes flowing in negative x-direction
outer = outer diameter
out = outgoing
part = particle: the dust or ash particles in the flue gas
rad, net = net radiation
right = right side of the superheater according to Fig. 2.3
s = steam
SH = superheater
sp = steampipe: the tubes containing the inner and outer steam
t = tubes
w = wall: the water tube walls in the cooling pass
water = saturated water in the water tube walls
x = given discrete cell
x-1 = cell above cell x
x+1 = cell below cell x
y = surfaces within the given cell
z = neighbouring surfaces just above and below the given cell

Abstract

In EfW (Energy from Waste) boilers, flue gases can create corrosion of the superheaters and economisers, caused by deposits of the melted ashes. Due to this, the flue gases are cooled with water wall panels and water tube walls in a cooling pass before reaching the heat transfer surfaces, thus limiting the power output. One way to increase the efficiency of the boiler is to introduce superheater screens in the cooling zone instead of using water wall panels to cool the flue gases. This new superheater would be covered in a ceramic material to protect its tubes from the above-cited fouling.

The purpose of the present work was to create a 1D model that describes the heat transfer from the flue gases to the coolant (steam and water) in the flue gas cooling pass of a power boiler. The 1D model, which is validated against CFD simulations using the Discrete Ordinates (DO) radiation model, will be used in the retrofit of EfW boilers. Furthermore, CFD simulations are used to study the pressure loss and mass flow distribution in the cooling pass under different situations and to provide design correlations. Also, the influence of different parameters on the computational cost of the CFD simulations is examined.

The 1D model agreed fairly well with the CFD simulation, especially in the lower part of the cooling pass. The flue gas outlet temperature was 4.5% lower in the 1D model than in the CFD simulation. In the 1D model, the geometry could be approached as rectangular canals, neglecting the inclination of the ceiling, and modelling the inlet and the outlet of the cooling pass as water tube walls. Regarding the flow field, the mass flow distribution in the cooling pass was found to be independent of factors such as the mass flow rate and the number of screens. It is sufficient to calculate the relative depths of the canals to get the mass flow distribution. The pressure loss can be found as a function of the average flue gas velocity in the cooling pass. The CFD mesh required approximately half a million cells, and the computational cost was decreased by using a symmetry plane in the middle of the cooling pass, costing just over an hour.

Keywords: Model, Heat Transfer, Radiation, CFD, Power Boiler, EfW, FBC

Sammanfattning

I sopeldade pannor kan rökgaserna orsaka korrosion på överhettare och ekonomiser på grund av askpåslag. Därför kyls rökgaserna i ett kylpass med vattenkylda väggar och vattenpanelväggar innan de når de värmeöverförande ytorna, vilket minskar pannans totala verkningsgrad. Ett sätt att öka pannans effektivitet är att byta ut vattenpanelväggarna till en överhettare uppdelad i ett antal skärmar, täckt med en keram för att skydda den från att korrodera.

Syftet med den aktuella studien var att skapa en 1D-modell som beskriver värmeöverföringen från rökgaserna till kylmediet (ånga och vatten), i rökgaskylkanalen i en kraftpanna. 1D-modellen, som valideras genom CFD-simuleringar med strålningsmodellen ”Discrete Ordinates”, kommer att användas vid ombyggnation av sopeldade pannor. CFD-simuleringar används dessutom för att undersöka tryckfallet och massflödesfördelningen i kylpasset under olika förhållanden och för att ta fram designkorrelationer. Olika parametrars inverkan på beräkningskostnaden undersöks också.

1D-modellen stämde någorlunda väl överens med CFD-simuleringen, speciellt i den lägre delen av kylpasset. Rökgastemperaturen vid utloppet var 4,5 % lägre i 1D-modellen än i CFD-simuleringen. I 1D-modellen kunde geometrin approximeras som rektangulära kanaler. Det lutande taket kunde försummas, och inloppet och utloppet kunde modelleras som vattenkylda väggar. Det visade sig att massflödesfördelningen i kylpasset var oberoende av faktorer som massflödeshastigheten och antalet skärmar. Det räcker att beräkna det relativa djupet på kanalerna för att kunna beräkna massflödesfördelningen. Tryckfallet i kylpasset kan beräknas som en funktion av rökgasens medelhastighet i kylpasset. CFD-meshen behövde ca en halv miljon celler. Beräkningskostnaden minskades genom att använda en symmetrilinje i mitten av kylpasset, vilket gjorde att kostnaden blev en dryg timma.

Nyckelord: Modell, värmeöverföring, strålning, CFD, kraftpanna, sopeldad panna, fluidiserad bädd-panna

Table of Contents

1. Introduction

1D models are often used for dimensioning heat transfer areas in power boilers. These models are usually based on correlations that can be found either in the literature, through experiments or with simulations using Computational Fluid Dynamics (CFD). CFD is often faster and less costly than carrying out experiments.

1.1. Background

In EfW (Energy from Waste) boilers, flue gases can create corrosion of the superheaters and economisers caused by deposits of the melted ashes. As the ashes are deposited on the heat transfer surfaces, the alkali chlorides of the ashes cause severe corrosion, especially if the ashes are melted [1]. This reaction increases with an increasing temperature, so in order to reduce the corrosion, the flue gases need to be cooled down from 850 ºC to around 650 ºC in a so-called empty cooling pass before reaching the superheaters [2], see Fig. 1.1. The cooling in the empty cooling pass is attained with tubes filled with saturated water, arranged in four chambers with water wall panels and water cooled walls. The cooling water is linked to the dome of the boiler.

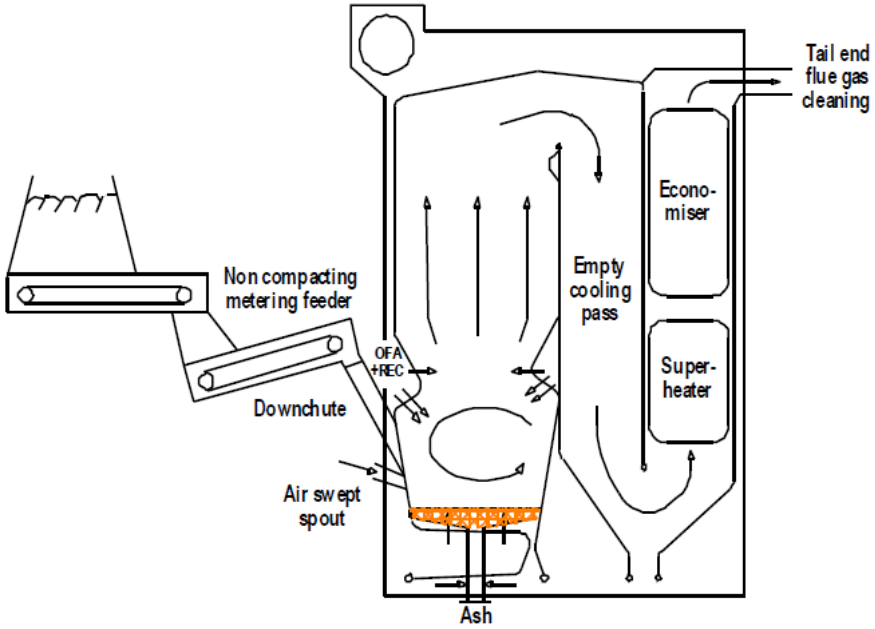

Figure 1.1. A scheme of an EfW boiler showing the empty cooling pass. [With permission from Jan Olofsson, Metso Power.]

However, the lower temperature of the flue gases as they reach the superheater section limits the maximum steam temperature, which in turn limits the maximum power output. One way to solve this is to introduce a superheater in the cooling zone instead of using water panels to cool the flue gases. This new superheater would be covered in a ceramic material to protect its tubes from the above-cited fouling. A share of the steam flow after the secondary superheater would be led back into the superheater in the empty cooling pass, thus increasing the steam temperature and thereby the power output.

Experiments have been conducted in a 20 MW EfW boiler in Borås where a superheater was added in the cooling section. The amount of ashes that accumulated on the

superheater was unexpectedly high, causing insulation and thus a lower steam temperature than expected. However, results from the experiments were sufficiently encouraging to continue the technology development and to investigate the system more thoroughly using a numerical tool.

1.2. Aim

The goal of the present work was to create a 1D model that describes the heat transfer from the flue gases to the coolant (steam and water) in the flue gas cooling pass of a power boiler. Metso Power will use this tool in the retrofit of EfW boilers.

Such a model can be then used for dimensioning and design of the heat transfer surfaces. The implementation of the model uses Scilab and is supported by CFD simulations (using FLUENT 13.0).

The relevant questions to be addressed in this study are:

- Is there any previous research in the area that might be relevant?
- How are the mass flow distribution and the pressure loss over the cooling pass affected by factors such as the mass flow rate and the number of screens?
- Were there any parts of the geometry that could be simplified?
- What physical phenomena are excluded from the simplest radiation models in FLUENT and how well did the results from the simulation using the radiation model agree with the results from the 1D model?
- Computational cost: how fine did the mesh need to be to give a sufficiently good solution? How long did each simulation take? Were there efficient ways to decrease the computational cost?

1.3. Scope

The study was limited to heat transfer calculations of the cooling pass of a specific boiler with given dimensions. The furnace before the cooling pass and the convective zone after were excluded. Inlet boundary conditions were supplied by Metso Power.

1.4. Methodology

This work has been divided into three parts:

- Literature study of previous research in the field and the physics of relevance for this work.
- Development, based on results from CFD simulations, of correlations describing how the flow field in the cooling pass depends on parameters such as the flue gas flow, the number of superheater screens and the distance between the screens. Study of the influence of the mesh size on the accuracy of the solutions and the computational costs of the CFD simulations.
- Development, implementation and validation of a 1D model for the dimensioning of heat transfer areas, based on the above-cited correlations. CFD is used as validation tool.

2. Theory

In this chapter, the relevant theory needed for the understanding of the present work is presented.

2.1. Fluidised Bed Units and Energy from Waste Boilers

The first fluidised bed (FB) units were developed in the beginning of the 20th century and they were used for coal combustion and gasification. Later they were used for catalytic reactions and, more recently, biomass and pre-treated waste have been used as fuels in FB combustion (FBC). The main advantages of FBC units over other combustion technologies are their fuel flexibility, their relatively uniform temperature distribution, low emissions of NO_x because of the lower operating temperature and the possibility of in-bed SO_x capture through limestone injection. Some of the main disadvantages of FBC units are the high dust content of the flue gases and that the combustion temperature is limited to around 900°C due to the risk of agglomeration of the bed material [3], [4].

The first applications for burning waste were built in Europe around 1890. Back then the main reason was hygienic: waste was burnt to reduce the risk of contagious diseases. After that, waste disposal was adopted. Today waste can be burnt to produce electricity and district heating, although waste incineration has high operational costs due to the need for flue gas treatment and residue management [3].

Most EfW boilers use grate burning, but since the 1980s the number of FBC boilers used to burn waste has increased. When burning waste in an FBC boiler there may be some problems with obstructions of the equipment, so the fuel needs to be treated prior to combustion. Alkali removal can be employed to reduce the risk for erosion and corrosion of the furnace walls and other heat transfer surfaces [3].

Compared to fossil fuels, waste has higher moisture and volatile content, more fragile structure, lower density and higher reactivity. These differences make the combustion behaviour of waste fuel different from that of fossil fuels. In an FBC boiler burning fossil fuels most of the combustion takes place in the dense bed, whereas for waste combustion a significant share of the volatile matter burns above the dense bed [3].

2.2. Computational Fluid Dynamics (CFD)

CFD is applied in several fields for the design, scale-up and optimisation of the modelled units. Within design and scale-up, CFD provides simulations of non-existing units, while within optimisation, CFD can be used instead of carrying out experimental work in the existing unit which can be costly and/or impossible to execute (for example because of the geometry of the system not allowing it).

2.2.1. Governing Equations

When using CFD, the studied domain is discretised into cells and the Navier-Stokes equations and the continuity equation (and optionally, the energy balance and the species balance) can be solved for each cell by means of e.g. the Finite Volume Method. This is done by rewriting these equations into discretised linear algebraic equations and

solving them for each cell in an iterative manner [5]. The continuity and Navier Stokes equations (Eqs. 2.1 and 2.2, respectively) are presented below: [6]

$$\frac{\partial \rho}{\partial t} + \nabla \cdot (\rho \vec{v}) = S_m \tag{2.1}$$

$$\frac{\partial}{\partial t}(\rho \vec{v}) + \nabla \cdot (\rho \vec{v} \vec{v}) = -\nabla \mathrm{p} + \nabla(\bar{\bar{\tau}}) + \rho \vec{g} + \vec{F} \tag{2.2}$$

The first terms on the left hand side (LHS) of Eqs. 2.1 and 2.2 describe the change in time of mass and momentum respectively, whereas the second terms describe the change in space. The term on the right hand side (RHS) of Eq. 2.1 is a source term whereas the terms on the RHS of Eq. 2.2 represent a pressure gradient, a shear stress gradient, the gravitational body force and external body forces.

The energy equation (Eq. 2.3) is also needed for the heat transfer simulations in this study: [6]

$$\frac{\partial}{\partial t}(\rho E) + \nabla(\vec{v}(\rho E + p)) = \nabla \cdot \left(k_{eff} \nabla T - \sum_j h_j \vec{J}_j + \left(\bar{\bar{\tau}}_{eff} \cdot \vec{v} \right) \right) + S_h \tag{2.3}$$

In Eq. 2.3 the first term on the LHS is the accumulation of heat, followed by the energy transfer through convection and expansion. On the RHS, the first term represents conduction, the second the energy transfer due to species diffusion followed by viscous dissipation and a source term.

In this work, the following assumptions and corresponding actions were taken:

- Reactions were assumed to be complete before reaching the empty cooling pass. Thus, the governing equation coupled to the species balance was not considered.
- Steady state was assumed. Thus, the accumulation terms in the governing equations were set to zero.
- The system modelled was assumed as single phase. Thus, there were no source terms to add to the governing equations.
- The gas was assumed to be perfectly mixed. Thus, there was no species diffusion.

2.2.2. Radiation Models

Radiation needs to be included in the modelling when the radiative heat flux is large compared to convection and conduction. This is the case when the gas temperature is high, i.e. at typical flue gas temperatures, since it will then give a large contribution due to its fourth-order dependence [6][1].

Figure 2.1 shows the different mechanisms of radiative heat transfer: emission from the gas, a scattering addition from the gas and losses from absorption and scattering.

[1] If no other reference is indicated, [6] is the reference for all equations and facts in Section 2.2.2.

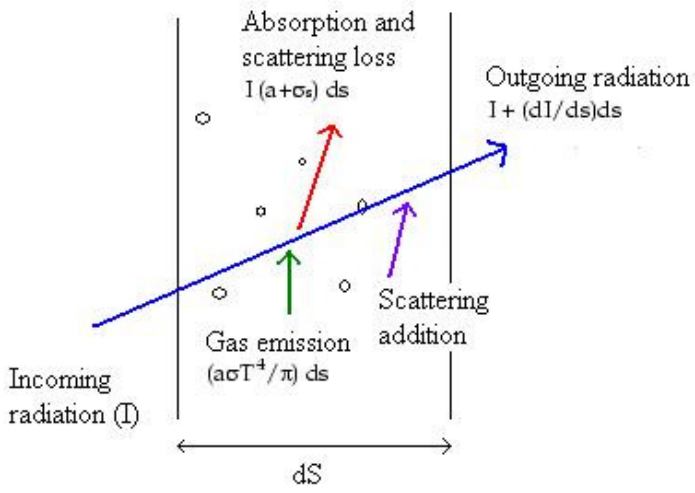

Figure 2.1. Radiative heat transfer mechanisms: gas emission, a scattering addition and absorption and scattering losses.

The radiative transfer equation is presented below:

$$\frac{dI(\vec{r},\vec{s})}{ds} + (a+\sigma_s)I(\vec{r},\vec{s}) = an^2\frac{\sigma T^4}{\pi} + \frac{\sigma_s}{4\pi}\int_0^{4\pi} I(\vec{r},\vec{s}')\,\Phi(\vec{s}\cdot\vec{s}')d\Omega' \tag{2.4}$$

The first term of Eq. 2.4 describes the change in radiation intensity over the distance s. The absorption and scattering losses are depicted by the second term. The third term includes the emission from the gas and in the final term the scattering addition is described. The phase function in the last term is a measure of the anisotropy of the scattering, see Eq. 2.5. It is set to 1 for purely isotropic scattering, which implies that the radiation intensity is the same in all directions [7].

$$\Phi(\vec{s}\cdot\vec{s}') = 1 + C\vec{s}\cdot\vec{s}' \tag{2.5}$$

In Eq. 2.5, C describes the anisotropy of the scattering. It ranges from -1 to1. Positive and negative values imply that more radiant energy is scattered forwards and backwards, respectively. When C is set to 0, isotropic scattering prevails.

To model the radiative transfer equation in FLUENT, five different radiation models can be used: the Discrete Transfer Radiation Model (DTRM), the P-1 Radiation Model, the Rosseland Radiation Model, the Surface-to-Surface (S2S) Radiation Model and the Discrete Ordinates (DO) Radiation Model. The advantages and limitations of all these models are briefly presented below. The DO model (see below) was chosen for the simulations in this work since it is the most flexible model.

The Discrete Transfer Radiation Model

In the DTRM it is assumed that a single ray can be used to approximate the radiation leaving a surface element, for a specific array of solid angles. There are three main advantages of the DTRM: it is a simple model, it can be used for a wide variation of optical thicknesses and by increasing the number of rays the accuracy can be increased.

Some important limitations are that scattering cannot be modelled and that grey (wave-length independent) radiation is assumed. All surfaces are assumed to be diffuse which implies isotropic reflection of the incident radiation. Also, simulating many rays can be computationally expensive.

The P-1 Radiation Model

The P-1 model is the simplest case of the P-N models, in which the radiation intensity is expanded into an orthogonal series of spherical harmonics. An additional transport equation is added in the P-1 model; the transport equation for the incident radiation, G.

An advantage of the P-1 model compared to the DTRM is that scattering is included, and it is possible to model anisotropic scattering. The radiative transfer equation (Eq. 2.4) is modelled as a diffusion equation which is easily solved at a low computational cost. The model works well for complicated geometries with curvilinear coordinates. Also, the model performs rather well for systems with a large optical thickness (e.g. mono-phase combustion applications).

There are some important limitations with the P-1 model. Grey radiation is assumed and all surfaces are assumed to be diffuse which implies isotropic reflection of the incident radiation. If the optical thickness is too small a loss of accuracy may occur which depends on the complexity of the geometry. Also, in the P-1 model there is a tendency that the radiative fluxes from localised sinks and sources of heat are overestimated.

The Rosseland Radiation Model

The Rosseland model bears some similarities with the P-1 model but instead of solving a transport equation for the incident radiation, G, black body radiation is assumed.

Since the Rosseland model does not solve an additional transport equation it is faster than the P-1 model. It also requires less memory. One limitation is that the Rosseland model only can be used for media that are optically thick. Also, it does not work with a coupled solver; a segregated solver must be used.

The Surface-to-Surface Radiation Model

In the S2S model it is assumed that there is no emission, absorption or scattering from the gas. It is suitable when the system consists of an enclosure of grey-diffuse surfaces, and a separating medium which do not affect the radiation between the surfaces. View factor calculations are carried out prior to simulations.

The main advantage of the S2S model is that its iterations are faster than for the other models (DTRM and DO), despite the computational cost of the view factor calculations. There are several important limitations: firstly, grey radiation is assumed and all surfaces are assumed to be diffuse. The model is only valid for unparticipating media. Surface clustering can be used to reduce the storage and memory needed for the simulations, but it does not decrease the time needed. Surface clustering does not work when dealing with sliding meshes or hanging nodes. The model is not valid if there are periodic or symmetry boundary conditions, and it does not work for 2D axisymmetric geometries. Finally the model only works for single enclosures, i.e. multiple enclosures cannot be treated with the S2S model.

The Discrete Ordinates (DO) Radiation Model.

The DO model solves Eq. 2.4 for a discrete number of solid angles linked to a fixed direction vector $\vec{s}$. The number of direction vectors equals the number of transport equations that are solved. In the DO model, Eq. 2.4 can be rewritten as:

$$\nabla \cdot (\mathrm{I}(\vec{r},\vec{s})\vec{s}) + (a+\sigma_s)I(\vec{r},\vec{s}) = an^2\frac{\sigma T^4}{\pi} + \frac{\sigma_s}{4\pi}\int_0^{4\pi} I(\vec{r},\vec{s}')\,\Phi(\vec{s}\cdot\vec{s}')d\Omega' \tag{2.6}$$

If non-grey (wave-length-dependent) radiation is to be modelled, a grey-band model is used and Eq. 2.6 becomes:

$$\nabla \cdot (\mathrm{I}_\lambda(\vec{r},\vec{s})\vec{s}) + (a_\lambda+\sigma_s)I_\lambda(\vec{r},\vec{s}) = a_\lambda n^2 \mathrm{I}_{\mathrm{b}\lambda} + \frac{\sigma_s}{4\pi}\int_0^{4\pi} I_\lambda(\vec{r},\vec{s}')\,\Phi(\vec{s}\cdot\vec{s}')d\Omega' \tag{2.7}$$

It is assumed that n, σ_s and $\Phi(\vec{s}\cdot\vec{s}')$ are wavelength independent, and that grey radiation prevails in each band. The radiation spectrum is divided up into N wavelength bands of the size $\Delta\lambda$ and integration is carried out over all the wavelength intervals. Transport equations for the radiant energy of each wavelength band, $I_\lambda\Delta\lambda$, are obtained. The total intensity is calculated by summation over the wavelength bands, i.e.

$$\mathrm{I}(\vec{r},\vec{s}) = \sum_{k=1}^{N} I_{\lambda k}(\vec{r},\vec{s})\lambda_{\mathrm{k}} \tag{2.8}$$

It is possible to model anisotropic scattering with the DO model. An isotropic phase function can be used, as well as a linear anisotropic phase function, a Delta-Eddington phase function or a user-defined phase function.

It is also possible to model particulate effects with the DO model. Scattering in the gas phase is neglected if particulate effects are included. In this case, Eq. 2.4 is rewritten as:

$$\nabla \cdot (\mathrm{I}\vec{s}) + \left(a+\mathrm{a_p}+\sigma_p\right)I(\vec{r},\vec{s}) = an^2\frac{\sigma T^4}{\pi} + \mathrm{E_p} + \frac{\sigma_p}{4\pi}\int_0^{4\pi} I(\vec{r},\vec{s}')\,\Phi(\vec{s}\cdot\vec{s}')d\Omega' \tag{2.9}$$

When modeling non-gray radiation, Eq. 2.9 is solved for each wavelength band considered. In the energy equation, particulate emission and particulate absorption are taken into account.

Boundary Conditions

For grey radiation the incident and outgoing radiative heat flux are defined according to Eqs. 2.10 and 2.11, respectively.

$$q_{in} = \int_{\vec{s}\cdot\vec{n}>0} I_{in}\vec{s}\cdot\vec{n}d\Omega \tag{2.10}$$

$$q_{out} = (1-\varepsilon_w)q_{in} + n^2\varepsilon_w\sigma T_w^4 \tag{2.11}$$

The radiation intensity at the wall is given by:

$$I_0 = \frac{q_{out}}{\pi} \tag{2.12}$$

For non-grey radiation, the boundary conditions are calculated in a similar way for each band considered. It is also possible to model semi-transparent walls with the DO model, but this is outside the scope of this work. The net radiative heat flux at inlets and outlets is approximated in the same way as that of the walls, using Eqs. 2.10 to 2.12.

Advantages and Limitations

Advantages of the DO model are that it is valid for the entire range of optical thicknesses, it can cover a wide variety of problems (e.g. radiation in semi-transparent media), it does not require a large amount of memory and it is relatively inexpensive in computational terms.

If the angular discretisation is very fine, the simulations may need a lot of computational power. The non-grey DO model can only be used when the spectral absorption coefficient of the participating media varies smoothly within each band. It is not possible to model the gas behaviour of gases absorbing or emitting energy at distinct wave numbers, such as carbon dioxide or water vapour. However, if the absorption coefficients within each band are assumed to be constant, it is possible to model such gases with this model.

2.3. Previous Research

Relatively much research has been carried out concerning CFD simulations of power boilers. There is still a limited (but increasing) amount of simulations made on FBC units and EfW boilers. Some of the more recent research of CFD simulations of power boilers relevant for this work is summarised below.

Ravelli et al. [3] modelled an FBC firing refuse-derived fuel (RDF), which involves some difficulties, partly due to the high variability of the heating value. Simulations were run for minimum load and maximum load and the solutions were compared with experimental data, yielding error values of the temperature field and the species concentration ranging from 0.1 to 6.7%, i.e. the overall the accuracy of the simulations was high.

Patil et al. [8] have conducted CFD simulations of a circulating fluidised bed (CFB) burning hazardous waste. The riser was modelled and its hydrodynamics, temperature and gas composition were resolved. The results could not be validated since the modelled CFB did not exist in reality.

Shah et al. [9] have also simulated a CFB in a study of the effect of the inlet and wall boundary conditions on the results. They modelled the case both in 2D and 3D. They studied three different types of boundary conditions for the 2-D simulations and found that the choice of boundary condition greatly influenced the results. Only one type of boundary condition was studied for the 3-D case and the results from this simulation as well as the results from one of the 2-D simulations agreed fairly well with experiments.

Phongphiphat et al. [10] used CFD to investigate corrosion of a superheater at high temperatures in a municipal solid waste plant. They found that temperature and particle

deposits greatly affected the rate of corrosion and this was validated with experimental results.

2.4. Description of the Cooling Pass

The flue gas enters and exits the cooling pass according to Fig. 2.2. The walls of the cooling pass are covered with water tube walls, containing saturated water, and thereby holding the same temperature all along the cooling pass. Some of this water is evaporated to steam but this part is so small that it can be neglected. The cooling pass is separated into a number of canals by superheater screens extending from the ceiling to the bottom of the cooling pass. The number of superheater screens can be varied; Fig. 2.2 shows a scenario with three superheater screens. The super heater screens are covered with a ceramic. They contain a number of concentric "double tubes" where the steam flows.

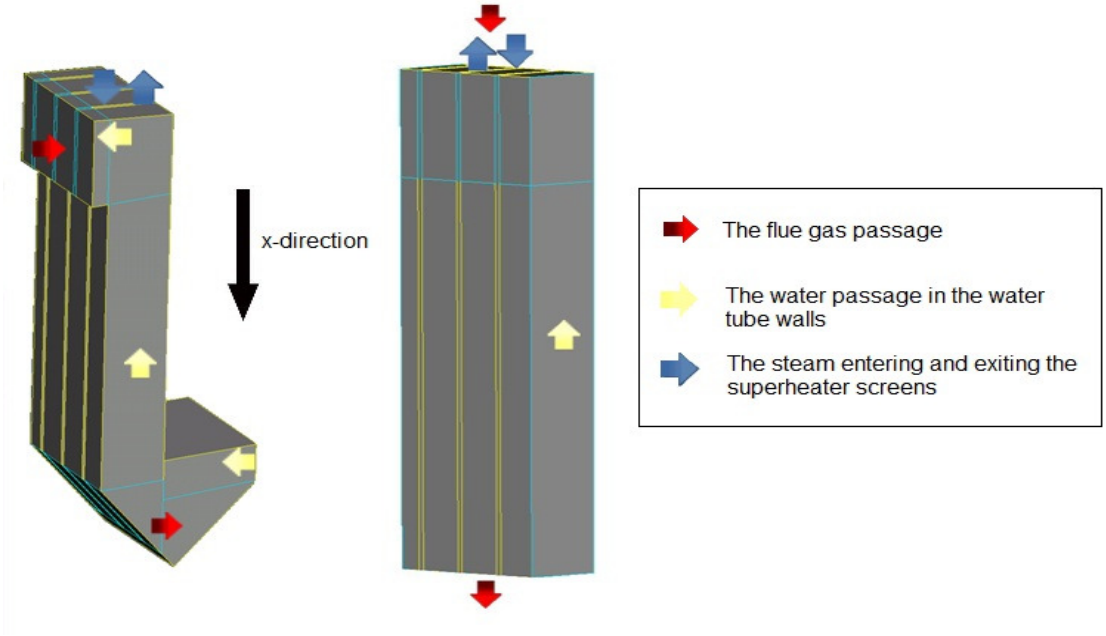

Figure 2.2. The cooling pass of the boiler, here with three superheater screens. To the left is the real geometry and to the right the simplified one described in the text. The figures are not to scale.

As mentioned above, data was supplied by Metso Power. The following parameters were given:

- The wet flue gas volumetric flow rate [Nm^3/s]
- The wet flue gas density [kg/Nm^3]
- The steam mass flow rate [kg/s]
- The flue gas composition [vol%]
- The dust density of the flue gas [g/Nm^3]
- The flue gas inlet temperature to the cooling pass [°C]
- The "inner" steam temperature entering the superheater screens [°C]
- The pressure of the steam entering the superheater screens [barg]
- The fouling resistance on the boiler tube walls [$W/m^2/K$]
- The fouling resistance on the superheater screen surfaces [$W/m^2/K$]
- Geometrical data used in the "base case" described in Chapter 3.

Some modifications of the geometry were made in the 1D model in order to simplify the radiation calculations, see Fig. 2.2 for comparison with the real geometry. The inlet of the cooling pass was treated as a water tube wall and so was the outlet, which was set to where the superheater screens ended. Also, the roof was considered horizontal. In these geometrical simplifications the removed area almost equalled the added area.

The following constraints were set to simulations of the cooling pass: the width of the cooling pass was not changed, although the depth (and thus the amount of superheater screens in the cooling pass) could be varied somewhat. The number of screens for a certain depth was limited due to the need for space for soot blowers and the risk of remains of the fuel getting trapped between screens.

2.5. 1D Modelling

The 1D model solves a set of three differential equations setting energy balances: for the temperatures of flue gas, inner steam and outer steam. The three modes of heat transfer (convection, conduction and radiation) are taken into account in the equations.

In Eq. 2.13, the change of the flue gas temperature in the x-direction (down the empty cooling pass, see Fig.2.2) is described in differential form. Equations in this section are written so that the reader can identify through negative signs the terms representing energy losses.

$$\dot{m}_{fg} C_{p,fg} \frac{dT_{fg}}{dx} = -U_{SH} A_{SH} \left(T_{fg} - T_{SH}\right) - U_w A_w \left(T_{fg} - T_w\right) + q_{rad\ net,fg} \tag{2.13}$$

In Eq. 2.13 the first two terms on the RHS represent heat transfer from the flue gases to the superheater screens and the water tube walls through convection. The third terms represents the net radiative heat transfer to the flue gas.

Equation 2.14 describes the change of temperature for the inner steam in the x-direction.

$$\dot{m}_s C_{p,is} \frac{dT_{is}}{dx} = U_{sp} A_{sp} (T_{os} - T_{is}) \tag{2.14}$$

The change of temperature of the inner steam is due only to its heat exchange with the surrounding outer steam. It is assumed that the heat transfer due to radiation is very small in this case, so only heat transfer through convection and conduction is included.

The equation for the temperature change of the outer steam in the x-direction is given below:

$$-\dot{m}_s C_{p,os} \frac{dT_{os}}{dx} = U_{SH} A_{SH} \left(T_{fg} - T_{SH}\right) - U_{sp} A_{sp} (T_{os} - T_{is}) + q_{rad\ net,SH} \tag{2.15}$$

The negative sign on the LHS term is explained by the outer steam flowing in the negative x-direction. The first and third terms on the RHS represent energy incomes from the flue gas, through convection and radiation respectively. The second term on the RHS stands for energy loss to the inner steam.

In Eqs. 2.13 to 2.15, U is the convective heat transfer coefficient and it is described in more detail in Section 2.5.1., while the net radiation flux $q_{rad\ net}$, is described in Section 2.4.2.

The flue gas and steam properties change with temperature (see App. A for further details). This is taken into account when solving Eqs. 2.13 to 2.15 by discretising the equations, which yield respectively:

$$T_{fg,x} = T_{fg,x-1} - \frac{1}{\dot{m}_{fg} C_{p,fg,x-1}} (U_{SH,x-1} A_{SH,\Delta x} \left(T_{fg,x-1} - T_{SH,x-1}\right) + U_{w,x-1} A_{w,\Delta x} \left(T_{fg,x-1} - T_w\right) - q_{net\ rad,fg,x}) \quad (2.16)$$

$$T_{is,x} = T_{is,x-1} + \frac{1}{\dot{m}_s C_{p,is,x-1}} U_{sp,x-1} A_{sp,\Delta x} \left(T_{os,x-1} - T_{is,x-1}\right) \quad (2.17)$$

$$T_{os,x} = T_{os,x-1} + \frac{1}{\dot{m}_s C_{p,os,x-1}} (-U_{SH,x-1} A_{SH,\Delta x} \left(T_{fg,x-1} - T_{SH,x-1}\right) + U_{sp,x-1} A_{sp,\Delta x} \left(T_{os,x-1} - T_{is,x-1}\right) - q_{rad\ net,SH,x}) \quad (2.18)$$

In Eqs. 2.16 to 2.18, the subscript x represents the value in the present cell whereas $x-1$ represents the value in the cell above. Equations 2.16 to 2.18 are solved for n equally long cells where $n = h/\Delta x$. The explicit Euler forward method is used to solve for $T_{fg,x}$, $T_{is,x}$ and $T_{os,x}$ for each discrete cell x.

Since the outgoing outer steam temperature, $T_{os,1}$, is unknown it must be guessed initially. The convergence criterions used are the inner and outer steam temperatures at the bottom of the empty cooling pass which ideally should be equal. Thus a tolerance δ is defined so that convergence is reached when $\left|T_{is,N} - T_{os,N}\right| \leq \delta$. This tolerance is set to 1K.

As mentioned above, the Euler forward method was used to solve the differential equations for the temperature, thus using the values in the previous cell to solve for the temperatures in the current cell, due to convergence issues. However, the net radiation used to calculate the new temperature is the net radiation in the current cell, and since the radiation contributes much more to the temperature than convection and conduction, this simplification should not affect the results very much. Also, by increasing the number of cells, this error decreases.

2.5.1. Convection and Conduction

The heat transfer coefficient, *U*, is used to quantify the heat transfer caused by convection and conduction. Note that since *U* does not include heat transfer by radiation it cannot be called the "overall heat transfer coefficient" when applied to superheater screens and water tube walls, since these surfaces are exposed to radiation. It depends on the inner and outer convective heat transfer coefficients, the conductive heat transfer coefficient and fouling coefficients (if fouling is an issue). In this section, the heat transfer coefficients for the superheater screens, the walls of the empty cooling pass and

the "steampipes" (the tubes containing the inner and outer steam in the superheater screens) are defined and explained in detail [11]. [2]

Heat Transfer Coefficient of the Superheater Screens

Two heat transfer coefficients of the superheater screens are defined for each screen: $U_{SH,left}$ and $U_{SH,right}$, see Fig. 2.3. They both include the convective heat transfer from the flue gases to the superheater screens $h_{fg,SH}$ and the fouling on the outer surface of the superheater screens, $h_{SH,fouling}$. U_{SH} is defined in Eq. 2.19, based on the outer surface of the superheater screens.

$$U_{SH} = \frac{1}{A_{SH}\left(\frac{1}{h_{fg,SH}A_{SH}} + \frac{1}{h_{SH,fouling}A_{SH}}\right)} \tag{2.19}$$

Here $A_{SH} = w\Delta x$ is the area of the superheater screen for each cell.

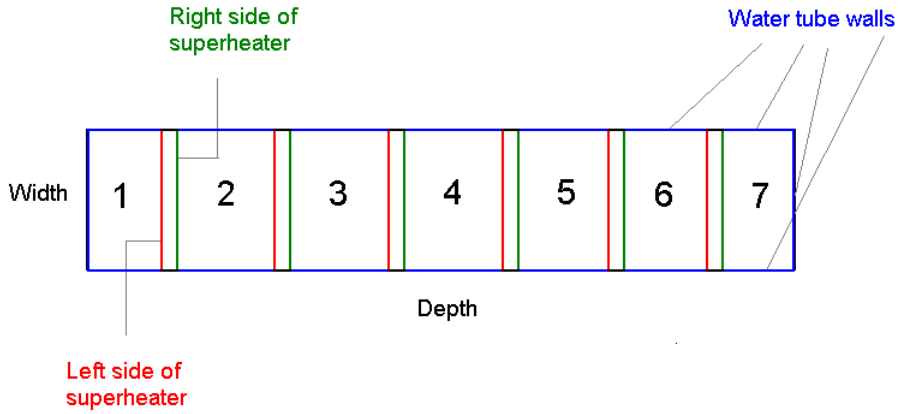

Figure 2.3. Cross section of the cooling pass seen from above showing a case with 6 superheater screens and seven flue gas canals. The figure is not to scale.

Convective Outer Heat Transfer Coefficient of the SH Screens, $h_{fg,SH}$

Since the superheater screens are shaped like thin cuboids, $h_{fg,SH}$ can be approximated with correlations for flow parallel to a plane surface, i.e.

$$h_{fg,SH} = \frac{Nu_L \lambda_{fg}}{L} \tag{2.20}$$

In Eqs. 2.20 and 2.21, the characteristic length, L, is taken as the hydraulic diameter of the flue gas canal. The Nusselt number is calculated as:

$$Nu_L = 0.036 Re_L^{4/5} Pr^{1/3} \tag{2.21}$$

The Reynolds number for the flue gases is defined according to:

[2] If no other reference is indicated, [11] is the reference for all equations and facts in Section 2.5.1.

$$Re_L = \frac{\rho_{fg} v_{fg} L}{\mu_{fg}} = \frac{\rho_{fg} \frac{\dot{m}_{fg}}{\rho_{fg} A_{cr}} L}{\mu_{fg}} = \frac{\dot{m}_{fg} L}{\mu_{fg} A_{cr}} \tag{2.22}$$

The Prandtl number for the flue gases is defined as:

$$Pr = \frac{\mu_{fg} C_{p,fg}}{\lambda_{fg}} \tag{2.23}$$

Convective Heat Transfer Coefficient of the Walls

The convective heat transfer coefficient for the walls includes the convective heat transfer from the flue gases to the water tube walls $h_{fg,w}$, the phase change taking place inside the boiling water tubes h_{water}, the conductive heat transfer of the steel of the tube walls λ_w and the fouling on the outer surface of the water tube walls, $h_{w,fouling}$. It is defined in Eq. 2.24a, based on the outer surface of the walls.

$$U_w = \frac{1}{A_{w,o}\left(\frac{1}{h_{fg,w} A_{w,o}} + \frac{1}{h_{w,fouling} A_{w,o}} + \frac{l_w}{\lambda_w} + \frac{1}{h_{water} A_{w,i}}\right)} \tag{2.24a}$$

Since only a small part of the water in the water tube walls undergoes a phase change, the heat transfer coefficient inside the water tubes is assumed to be much larger than the other terms in Eq. 2.24a, so the resistance $1/h_{water} A_{w,i}$ is neglected. The conductive heat transfer is neglected compared to that of convective heat transfer. With this, Eq. 2.24a becomes:

$$U_w = \frac{1}{\frac{1}{h_{fg,w}} + \frac{1}{h_{w,fouling}}} \tag{2.24b}$$

Convective Outer Heat Transfer Coefficient of the Water Tube Walls, $h_{fg,w}$

The water tube walls are approximated as parallel, plane surfaces. The convective outer heat transfer coefficient for the walls then becomes equal to the convective outer heat transfer coefficient for the superheater screens:

$h_{fg,w} = h_{fg,SH} = h_{fg}$

Overall Heat Transfer Coefficient of the Steampipe

The overall heat transfer coefficient for the steampipe includes the convective heat transfer from the hot steam to the steampipe $h_{os,sp}$, the convective heat transfer from the cold steam in the internal tubes inside the superheater screens to the steam pipe $h_{is,sp}$ and the conductive heat transfer of the steampipe λ_{sp}. Based on the outer area of the inner tubes, it is defined according to:

$$U_{sp} = \frac{1}{A_{sp,o,inner}\left(\frac{1}{h_{os,sp}A_{sp,o,int}} + \frac{ln\frac{D_{i,outer}}{D_{i,inner}}}{2\lambda_{sp}\pi\Delta x} + \frac{1}{h_{is}A_{sp,i,inner}}\right)} \quad (2.25a)$$

which after rearranging becomes:

$$U_{sp} = \frac{1}{\frac{1}{h_{os,sp}} + \frac{D_{i,outer}n_t ln\frac{D_{i,outer}}{D_{i,inner}}}{2\lambda_{sp}} + \frac{D_{i,outer}/D_{i,inner}}{h_{is}}} \quad (2.25b)$$

Convective Outer Heat Transfer Coefficient of the Steampipe, $h_{os,sp}$

The convective outer heat transfer coefficient of the steampipe is approximated to be the same as the convective heat transfer coefficient for flow in a cylinder; the fact that there is an inner tube inside the outer tube is neglected. Then $h_{os,sp}$ can be written as:

$$h_{os,sp} = \frac{Nu_{D,os,t}\lambda_{os}}{L} = \frac{Nu_{D,os,t}\lambda_{os}}{D_{o,inner}} \quad (2.26)$$

The Dittus-Boelter equation can be used to describe Nu_D in this case.

$$Nu_{D,os,t} = 0.023Re_{D,os,t}^{0.8}Pr_{os}^{0.4} \quad (2.27)$$

The Reynolds and Prandtl numbers for the outer steam are defined respectively as:

$$Re_{D,os,t} = \frac{\dot{m}_{os,t}}{\mu_{os}\pi D_{o,inner}} \quad (2.28)$$

$$Pr_{os} = \frac{\mu_{os}C_{p,os}}{\lambda_{os}} \quad (2.29)$$

Convective Inner Heat Transfer Coefficient of the Steampipe, $h_{is,sp}$

The convective inner heat transfer coefficient for the steampipe is defined as:

$$h_{is,sp} = \frac{Nu_{Di,is,t}\lambda_{is}}{D_{i,inner}} \quad (2.30)$$

The Dittus-Boelter equation (Eq. 2.27) can once again be used to describe Nu_D. In this case the Reynolds number and the Prantl number for the inner steam are defined as:

$$Re_{D,is,t} = \frac{4\dot{m}_{is,t}}{\mu_{is}\pi D_{i,inner}} \quad (2.31)$$

$$Pr_{is} = \frac{\mu_{is}C_{p,is}}{\lambda_{is}} \quad (2.32)$$

2.5.2. Radiation

In this section, the expressions and assumptions used to model radiation in the 1D model are introduced. The modelling includes gas-surface, surface-surface and gas-gas radiation, also between non-neighbouring cells.

Net Radiation to the Flue Gas and the Superheater Screens

The temperature contribution to the flue gas and the hot steam through radiation is included in Eqs. 2.13 to 2.18 as a net source, $q_{net,rad}$.

Net Radiative Energy to the Gas Volume in a Cell

It is assumed that the gas can be modelled as a grey gas. In the 1D model, cells are regular hexahedra. Cell faces are assumed to radiate in the normal direction. Cell faces have a view factor of 1 to adjacent solid surfaces, whereas cell sides facing up or down, i.e. adjacent to other cells, radiate according to the expressions given below, see Figs. 2.4 and 2.5.

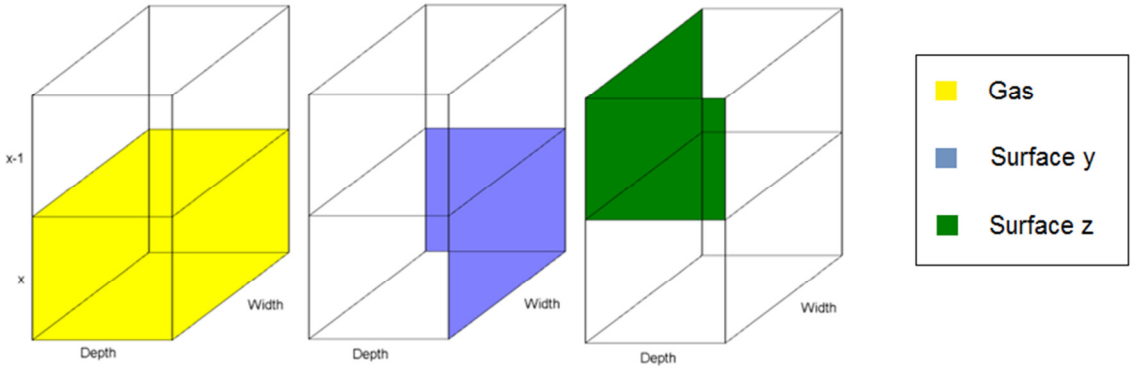

Figure 2.4. The figure to the left shows the gas volume of cell x. The middle figure shows two of the adjacent surfaces within the cell and the third shows two of the adjacent surfaces of the neighbour cell x-1.

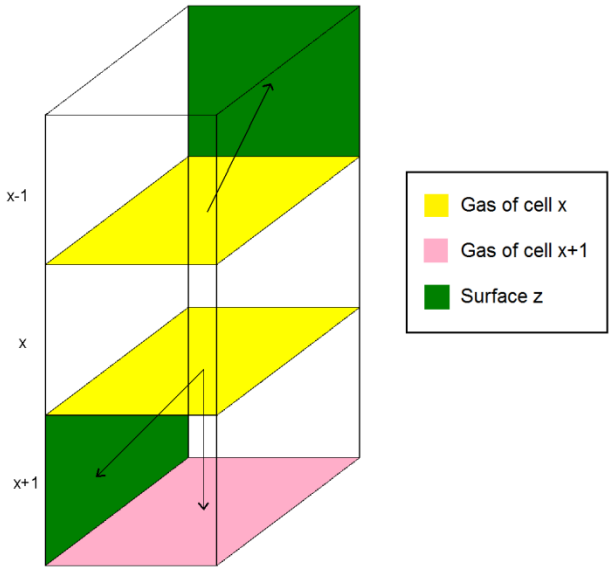

Figure 2.5. The top and bottom of the "gas hexahedra" of cell x (with the area A_g), radiating to two arbitrary adjacent surfaces of the neighbouring cells, and to the bottom of the gas hexahedra in cell x+1. The gas of cell x also radiates to the top of the gas hexahedra in cell x-1 but this is not shown here.

Radiation leaving the gas in cell x can be written as:

$$q_{fg,out,x} = \sigma T_{fg,x}^4 \left(\sum_y \varepsilon_{gy,x} A_y + \sum_z \varepsilon_{gz,x} F_{gz} A_g + 2F_{gg} A_g \varepsilon_{gg,x} \right) \tag{2.33}$$

In Eq. 2.33, y represents the surfaces enclosing the gas within the cell x, whereas z stands for the adjacent surfaces of the neighbour cells $x-1$ and $x+1$, see Fig. 2.4. Thus, the first term on the RHS describes the gas radiation to the surfaces within the cell, with a view factor of 1 since these are represented by the same surfaces, see Fig. 2.4. (The expressions used to calculate the view factor are found in App. B.) The second term represents the gas radiation to the adjacent surfaces of the neighbour cells and the third term describes the gas radiation to the gas of the cell above and below the present cell, see Fig.2.5.

The incoming radiation to the gas in cell x consists of the radiation from the flue gas in the previous and next cell, as well as the absorbed radiation in present cell, i.e.

$$\begin{aligned} q_{fg,in,x} &= \sigma A_g F_{gg} (\varepsilon_{gg,x+1} T_{fg,x+1}^4 + \varepsilon_{gg,x-1} T_{fg,x-1}^4) \\ &+ \sum_i \sum_j (\varepsilon_j \sigma T_j^4 + G_j (1-\varepsilon_j) F_{ji} A_j \alpha_{g,ji} \varphi_{ji,x}) \\ &+ \sum_y \left(\varepsilon_{gy,x-1} \sigma T_{g,x-1}^4 F_{gy,x-1} A_g \alpha_{gy,x} + \varepsilon_{gy,x+1} \sigma T_{g,x+1}^4 F_{gy,x+1} A_g \, \alpha_{gy,x} \right) \end{aligned} \tag{2.34}$$

In Eq. 2.34, the first term on the RHS represents the gas radiation from the previous and the next cells to the gas in the present cell, see Fig. 2.6. The second term represents absorption of the gas in the present cell, x, from all the surface-surface radiation taking place, see Fig. 2.7. $\varphi_{ji,x}$ is the fraction of radiative heat absorbed by the gas in cell x, see App. C for its definition. The final two terms stand for the absorption taking place when

the gas in the previous and next cells radiate to the surfaces enclosing the gas in the present cell, see Fig. 2.8.

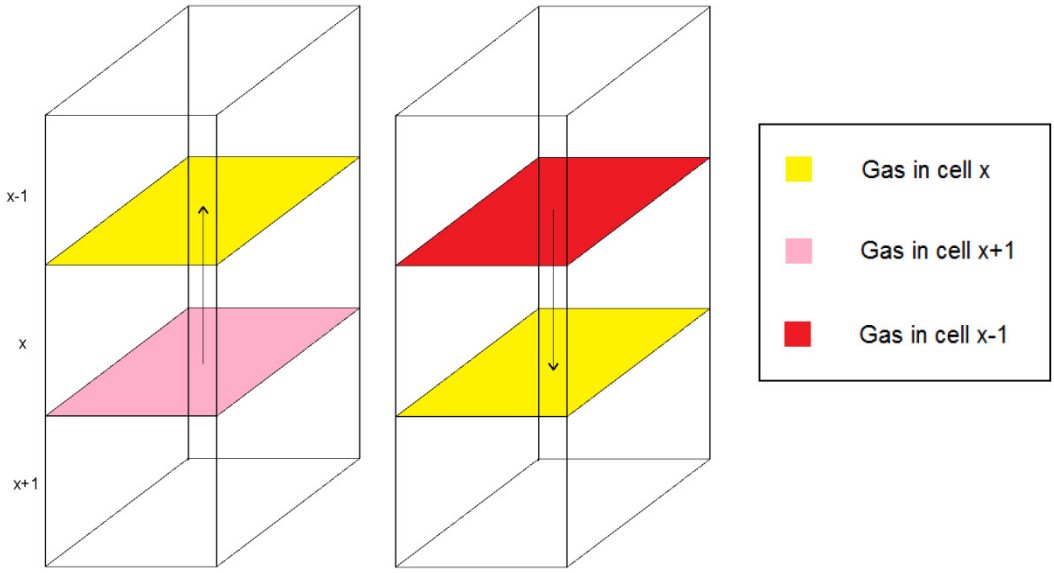

Figure 2.6. Gas-gas radiation, from the adjacent cells to cell x. The figure to the left shows the top of the gas box of cell x+1 radiating to the top of the gas box of cell x, whereas the figure to the right shows the bottom of the gas box of cell x-1 radiating to the bottom of the gas box of cell x.

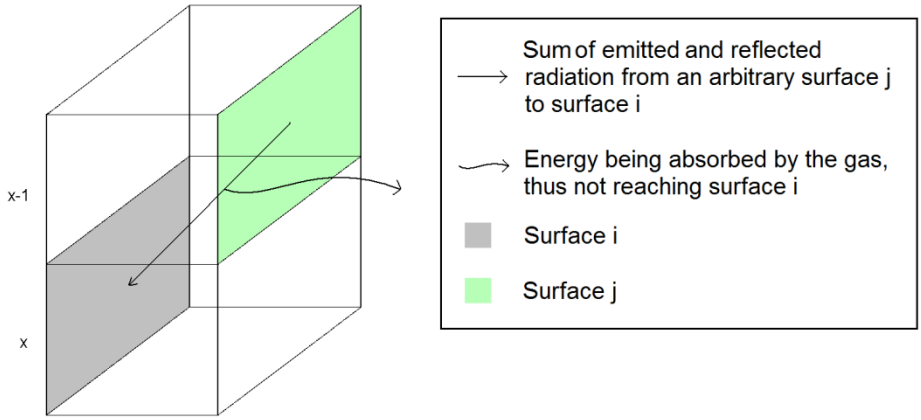

Figure 2.7. Radiation from an arbitrary surface j (this surface can be in any cell, not just the adjacent cells) to surface i in cell x. Part of this radiation gets absorbed by the gas in the cells that it passes.

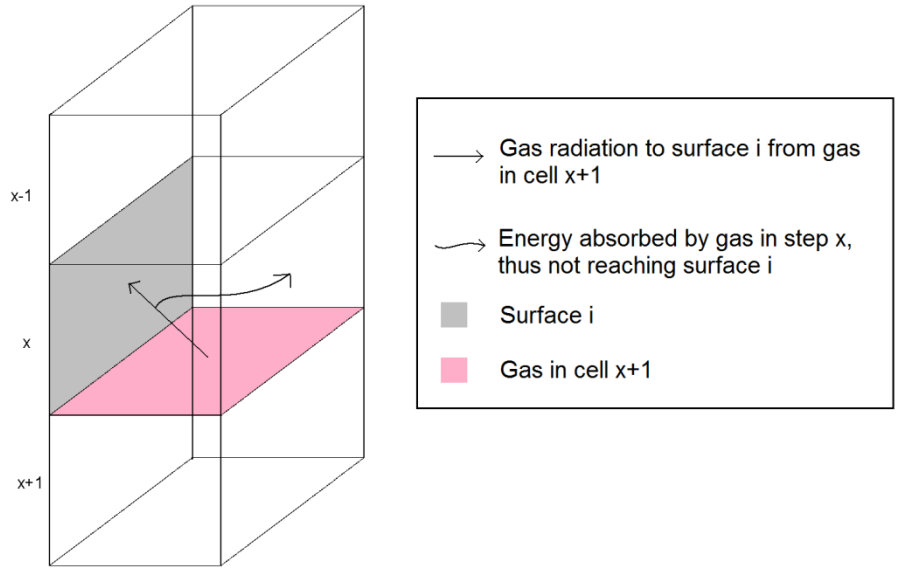

Figure 2.8. Gas radiation from cell x+1 to surface i in cell x. A fraction gets absorbed by the gas in cell x, and does not reach surface i. The gas in cell x-1 also radiates to surface i, but this is not shown.

Finally $q_{net,fg,x}$ is expressed as:

$$q_{net,fg,x} = q_{fg,in,x} - q_{fg,out,x} \tag{2.35}$$

Modelling the gas as a hexahedron is a simplification, since all gas molecules radiate in all directions. However, it should be a rather good model since it includes radiation in its own cell, to the gas in the adjacent cells and to the surfaces in the adjacent cells, so gas radiation in 14 different directions is actually included. To increase the accuracy of the model, radiation in more directions should be included, but this would also make the model much more computationally expensive.

The gas absorption during surface-surface radiation is divided evenly between the cells it passes through. This is not correct since the absorption actually should decay exponentially. However, it is necessary to make this simplification since the model would grow much more complex if this is to be included, and it would also make the 1D model more computationally expensive.

The gas is modelled as grey and no scattering is included, since it would have been extremely complicated to include non-grey radiation and scattering in a 1D model. Since there are ash particles in the gas mixture, scattering could be an issue and this could affect the results to a certain degree. Radiation from water vapour and carbon dioxide is wave-length dependent, so assuming that the gas can be modelled as a grey gas could also have an effect on the results, although it is difficult to say how big it could be.

Net Radiative Energy to the Superheater Screen in a Cell

For a given cell, x, the net radiation to the superheater screen is defined according to Eq. 2.36 (see also Fig. 2.9):

$$q_{rad,net,SH,x} = G_{SH,x}A_{SH,\Delta x} - G_{SH,x}A_{SH,\Delta x}(1-\varepsilon_{SH}) - \varepsilon_{SH}\sigma T_{SH,x}^4 A_{SH,\Delta x} = \\ = G_{SH,x}A_{SH,\Delta x}\varepsilon_{SH} - \varepsilon_{SH}\sigma T_{SH,x}^4 A_{SH,\Delta x} \quad (2.36)$$

In Eq. 2.36, the first term on the RHS represents the total incoming radiation, from the gas and the other surfaces in the enclosure. The second term represents the part of the incoming radiation that is reflected and the third term describes the emitted radiation from the superheater screen of cell x. Since the temperature of the superheater screen differs from the outer steam temperature, it is necessary to calculate the superheater screen temperature, $T_{SH,x}$. It is solved by rewriting Eq. 2.37, solving for $T_{SH,x}$.

$$q_{rad,net,os,x} + h_{fg,x}A_{SH,\Delta x}(T_{fg,x} - T_{SH,x}) = \frac{1}{\frac{1}{h_{os,SH,x}} + \frac{l}{\lambda_{SH}}} A_{SH,\Delta x}(T_{SH,x} - T_{os,x}) \quad (2.37)$$

Equation 2.37 states that the net heat of radiation and the heat by convection of the flue gases that enter the superheater surface in a given cell x is the same as that which is led away by conduction through the superheater screens and by convection to the outer steam. Figure 2.9 shows the different radiation fluxes and temperatures.

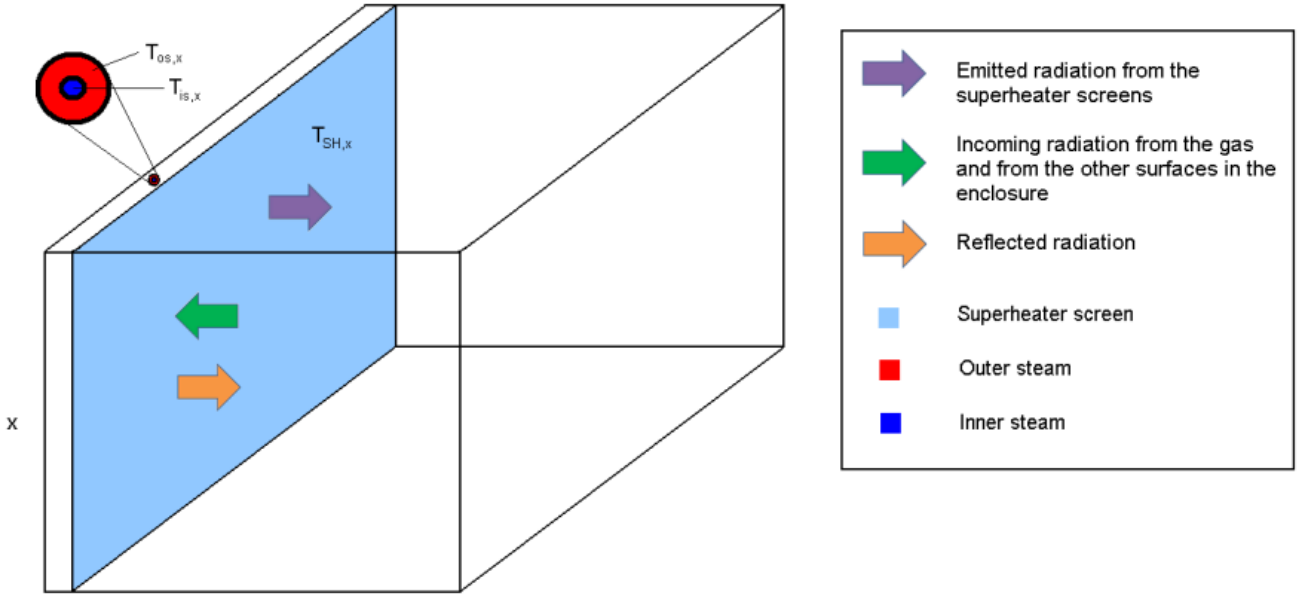

Figure 2.9. The radiation fluxes described by Eq. 2.36. The figure also shows one double tube.

In Eq. 2.38, $G_{i,x}$ is the incoming radiative flux to surface i in cell x. This is a function of the radiation leaving all other surfaces, j, through emission and reflection, the view factor between these surfaces and the studied surface i, the gas absorptivity and the incident gas radiation on surface i. It can be described as:

$$q_{in,i} = G_i A_i = \sum_j ((\varepsilon_j \sigma T_j^4 + G_j(1-\varepsilon_j)) \times F_{ji} A_j (1-\alpha_{g,ji})) + \varepsilon_{gi,x} \sigma T_{g,x}^4 F_{gi,x} A_g$$
$$+\varepsilon_{gi,x-1} \sigma T_{g,x-1}^4 F_{gi,x-1} A_g (1-\alpha_{gi,x}) + \varepsilon_{gi,x+1} \sigma T_{g,x+1}^4 F_{gi,x+1} A_g (1-\alpha_{gi,x}) \quad (2.38)$$

The first and second terms on the RHS of Eq. 2.38 represent the radiation incident on surface i from all other surfaces, see Fig. 2.7. These terms are multiplied by $(1-\alpha_{g,ji})$ to take into account the fact that some of the radiation is absorbed by the gas on the way and does not reach surface i, as shown in Fig 2.7. The third term describes the gas radiation to surface i within the cell, with a view factor of 1 since these are represented by the same surface, as stated above, see Fig. 2.4. The final two terms in Eq. 2.38 represent the gas radiation to surface i from the cells above and below, see Fig 2.8. These two terms also take into account the gas absorption along the gas path.

The absorptivity is set equal to the emissivity, according to Kirchhoff's law. The gas emissivity depends on the gas temperature, the partial pressures of water vapour and carbon dioxide and the mean beam length of radiation, as explained in more detail in App. C.

2.5.3. Pressure Drop in the Superheater Screens

The pressure drop in the tubes in the superheater screens can be found with correlations from the literature. The pressure drop in the tubes can be divided into the pressure drop caused by the friction between the steam and the pipe and into losses that occur at the inlet, the outlet and when the steam makes a U-bend. The total pressure drop in a tube can be calculated according to: [11]

$$\Delta P_t = 2 f_f \frac{L}{D} v^2 \rho + \frac{K_{inlet} v^2 \rho_{inlet}}{2} + \frac{K_{U-bend} v^2 \rho_{U-bend}}{2} + \frac{K_{outlet} v^2 \rho_{outlet}}{2} \quad (2.39)$$

The friction factor for smooth tubes can be found by solving for f_f in Eq. 2.40. [11]

$$\frac{1}{\sqrt{f_f}} = 4.06 \times \log_{10}\left(Re\sqrt{f_f}\right) - 0.60 \quad (2.40)$$

The friction loss factors in Eq. 2.39 are presented in Table 2.1.

Table 2.1. Friction loss factor for losses occurring at the inlet, the outlet and when the steam makes a U-bend at the bottom of the cooling pass [11], [12].

	Inlet	U-bend	Outlet
Friction loss factor [-]	0.5	1.6	1

3. Method

As mentioned in Section 1.4, the present study consisted of three different parts and therefore this chapter is also divided into three parts: the literature study, the CFD-simulations and the creation of the 1D model.

3.1. Literature Study

Initially, specific theoretical and background knowledge was acquired through a literature study. Scientific articles, the FLUENT user manual, textbooks and websites were used.

3.2. CFD Simulations

This section describes the preparations that were necessary before starting the CFD simulations (creation of geometries and meshes, generation of inlet velocity profiles and implementation of user-defined functions for the flue gas properties) and the simulation matrix adopted.

3.2.1. Creating the Geometry and Mesh

Before carrying out the actual CFD-simulations in FLUENT, the geometry needed to be created and meshed. ANSA was used for this purpose. The boiler design in paper format was provided by Metso Power. After measuring and scaling the necessary dimensions, the geometry (from now on called the base case geometry) was created in ANSA.

Since the heat exchange modelled in CFD concerned exclusively that between gas and surfaces (i.e. not within the screens or tubes), only the walls of the superheater screens were included in the geometry. For the CFD simulation that included heat transfer, the temperature at the surface of the superheater screens was imported from result data provided by the 1D model. This specific CFD simulation was mainly carried out to check the validity of the radiation model in the 1D model.

The outlet was elongated to avoid inaccuracies caused by backflow. Interior surfaces were also created in some places since they were needed for the volume meshing. Due to symmetry, only half of the geometry needed to be analysed.

The mesh was mostly structured except for in some places where it was not possible to create a structured mesh. However, these areas were not considered to significantly affect the results of the simulations.

The mesh was made by first setting the number of nodes for each edge of the geometry. This was done in such a way that as many volume cells as possible would be hexahedrons. y^+ adaption was applied at the walls. The distance to the first cell was approximated using an online grid spacing calculator [13]. The surface mesh was then created using quadrilateral mapping. For some parts of the geometry it was impossible to generate only quadrilaterals so for these parts the Free algorithm was used, which creates mostly unstructured quadrilaterals but at those areas where that is not possible it creates triangles. When the surface mesh was complete, the volume mesh was created with volume mapping. The final volume mesh was made up of hexahedrons except for

in those places where the Free algorithm had been used. These parts of the volume mesh included some pentahedrons.

For the simulations using the Discrete Ordinates Radiation Model, the base case geometry was used. However, it needed to be re-meshed, using y^+-adaption of 1 at the walls of so as to fully resolve the heat transfer taking place at these zones. This mesh contained approximately 1 million cells.

3.2.2. Further Preparations for the Simulations

Since the cooling pass is situated after the combustion zone, the flow can be assumed to be fully turbulent when reaching the inlet of the cooling pass. This was achieved by using the inlet geometry described above and setting its outlet as a periodic inlet and running the simulation until it converged. The Realizable k-ε model was used in this simulation.

When running simulations with the energy equation on, it was necessary to include models for the viscosity, the density, the specific heat capacity and the thermal conductivity of the flue gases. The temperature dependence of the specific heat capacity was written as a polynomial in FLUENT. The temperature dependence of the other three properties was included in FLUENT by the use of three UDFs (user defined functions). The equations described in App. A were used for all four properties.

The temperature of the superheater screens was imported into FLUENT as a 1D profile generated by the 1D model.

3.2.3. Simulation Matrix

CFD simulations were carried out in order to study the computational costs, create correlations for both the mass flow distribution and the pressure loss in the cooling pass and to validate the 1D model.

Three different parameters were varied in order to create the mass flow distribution and pressure loss correlations: the mass flow, the number of superheater screens and the distance between the superheater screens.

Varying mesh size

To study computational costs and the optimal mesh size, a base geometry consisting of six superheater screens was first created. This geometry was based on the boiler drawing supplied by Metso Power. The mesh of this case was made in three levels of coarseness that are here named “coarse”, intermediate” and “fine” and whose main characteristics are seen in Table 3.1.

Table 3.1. The main characteristics of the three meshes used to study computational costs.

Mesh	Coarse	Intermediate	Fine
Spacing factor	1.5	1.2	1.125
Number of cells	94 354	570 908	1 078 854
y^+ adaption	30-100	30-100	30-100

Varying Geometry

In order to study the influence on the mass flow distribution and pressure drop, the geometries given below were also created and meshed using the criteria for the above-given "intermediate" mesh:

- One geometry with all depths 50% longer than the depths of the base case, with six superheater screens.
- One geometry with all depths 50% shorter than the depths of the base case, with six superheater screens
- One geometry with the same distances between the superheater screens and the water tube walls as the base case but with 4 superheater screens.
- One geometry with the same distances between the superheater screens and the water tube walls as the base case but with 5 superheater screens.
- 2 different geometries where the depth of the fourth canal was made 100% larger and 50% smaller than in the base case, both with six superheater screens
- 2 different geometries where the depth of the first (and last, due to symmetry) canal was made 100% larger and 50% smaller than in the base case, both with six superheater screens
- The inlet of the cooling pass made a few cells wide for the creation of a periodic inlet as described below. This was made for each different geometry of the cooling pass.

Varying the Mass Flow

To see how the flow field was affected by the mass flow rate, simulations were run for the base case geometry discretised with the intermediate mesh. Three different mass flow rates of the flue gas were studied. Simulations were made for 50%, 100% and 150% of the given flue gas flow rate. All other factors were kept constant in these simulations.

First the different inlet velocity profiles were created for each mass flow rate simulation. The density and the viscosity were assumed to be constant all along the domain and were evaluated at $\frac{T_{fg,in}+T_{fg,out,guess}}{2}$.

The different mass flow simulations were all run at steady state, single phase and with the energy equation turned off. The turbulence model that was used was the Realizable k-ε model with enhanced wall functions. A pressure-based solver was used and the SIMPLE algorithm was used to deal with the pressure-velocity coupling.

The velocity magnitude of the inlet velocity profile was set as the inlet velocity boundary condition. Also, the turbulent intensity at the inlet was set to 10% and the hydraulic diameter was used to estimate the turbulent length scale. The outlet was set as a pressure outlet with the same turbulent intensity, and the turbulent length scale was estimated from the hydraulic diameter of the outlet. The no slip condition was used at the walls.

The first order upwind scheme was first used as the solution method. When the solution had converged, the second order upwind scheme was employed to increase the accuracy

of the solution. To check for convergence, the mass flow at the outlet and the sum of the velocity magnitude for a created plane were monitored, as well as the residuals.

Simulation with the Discrete Ordinates Radiation Model

One simulation was run using the Discrete Ordinates Radiation Model to validate the 1D model, using the mesh with a y^+ adaption of 1 at the walls, described in Section 3.2.1. The turbulence model used was the same as above. Grey radiation was assumed and no scattering was included. The absorption coefficient of the flue gas was described as piecewise-linear. The boundary conditions for the flow field were the same as described above. The temperature of the water tube walls was set constant and a temperature profile was set at the surface of the superheater screens.

Convergence was checked for by monitoring the sum of velocities and the sum of temperatures at a plane, as well as checking the residuals.

3.3. 1D Model

The 1D model was first implemented in MATLAB. To simplify the procedure and make it easier to detect mistakes, only the convective and conductive heat transfer was solved to begin with. When this worked the radiation model was added gradually. Code routines are described in detail in Chapter 4.

When the MATLAB code was complete, it was converted to Scilab code (an open-source program), which was then coupled to Excel using Xls-link, so that the inputs and the results could be entered and displayed in an Excel spreadsheet.

The 1D radiation model was validated using the results from the CFD run with the DO radiation model, by comparing the flue gas outlet temperature in the two cases and the incident radiation on the superheater screens. This is given in Section 4.3.1.

Finally, a sensitivity analysis was carried out where the number of discrete cells and some of the most uncertain input parameters were varied: the wall emissivities and the convective heat transfer coefficient of the flue gas. This is given in Section 4.3.2.

4. Results and Discussion

This chapter has been divided into the results from the CFD simulations and the resulting 1D model, including validation of the 1D model.

4.1. Results from CFD Simulations

Several flow field simulations were carried out, where different issues were investigated. The results from these simulations are presented in this section.

4.1.1. Mesh Study

As presented in Section 3.2.3., three different meshes were examined and the results are summarised in Tables 4.1 and 4.2. The differences in mass flow in Table 4.2 were calculated according to:

$$Difference = \frac{\dot{m}_{intermediate} - \dot{m}_{coarse,fine}}{\dot{m}_{intermediate}} \quad (4.1)$$

Table 4.1. Comparison of the simulation time for the three different meshes.

Mesh	Coarse	Intermediate	Fine
Number of cells [-]	94 354	570 908	1 078 854
Simulation time [min]	33	74	157
Time/iteration [s/iteration]	0.5	3.4	6.7

Table 4.2. Difference in mass flow rate in each canal for the different meshes.

Comparison	Coarse-Intermediate	Fine-Intermediate
Difference canal 1&7 [%]	1.21	0.282
Difference canal 2&6 [%]	0.482	-0.200
Difference canal 3&5 [%]	1.27	0.0757
Difference canal 4 [%]	2.29	0.0361

As shown in Tables 4.1 and 4.2, the simulation with the coarse mesh was the fastest but when compared to the mass flow of the intermediate mesh it differed by as much as 2.29% for canal 4. The simulation with the fine mesh took the longest, although 157 minutes is not an extremely long time considering how big the geometry is. When compared to the intermediate mesh the differences in mass flow rates are much smaller than for the coarse mesh. The largest difference occurred in canals 1 and 7 and it was only 0.282%. Figures 4.1 and 4.2 show the difference of the velocity contours for the intermediate mesh and the coarse mesh, and the intermediate mesh and the fine mesh, respectively.

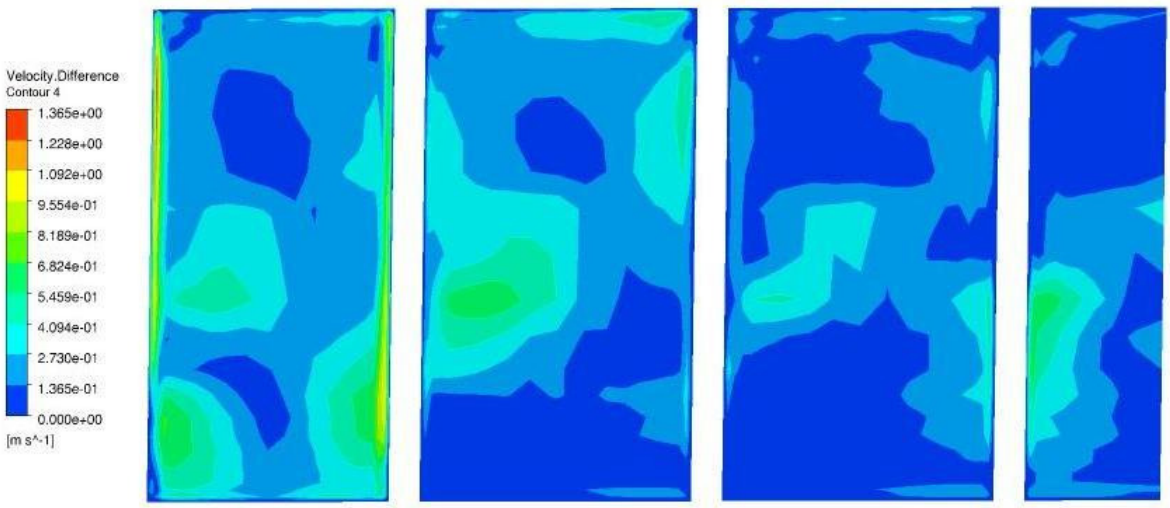

Figure 4.1. The differences in velocity for the intermediate mesh and the coarse mesh. There is a symmetry plane in the middle of the fourth canal (right end).

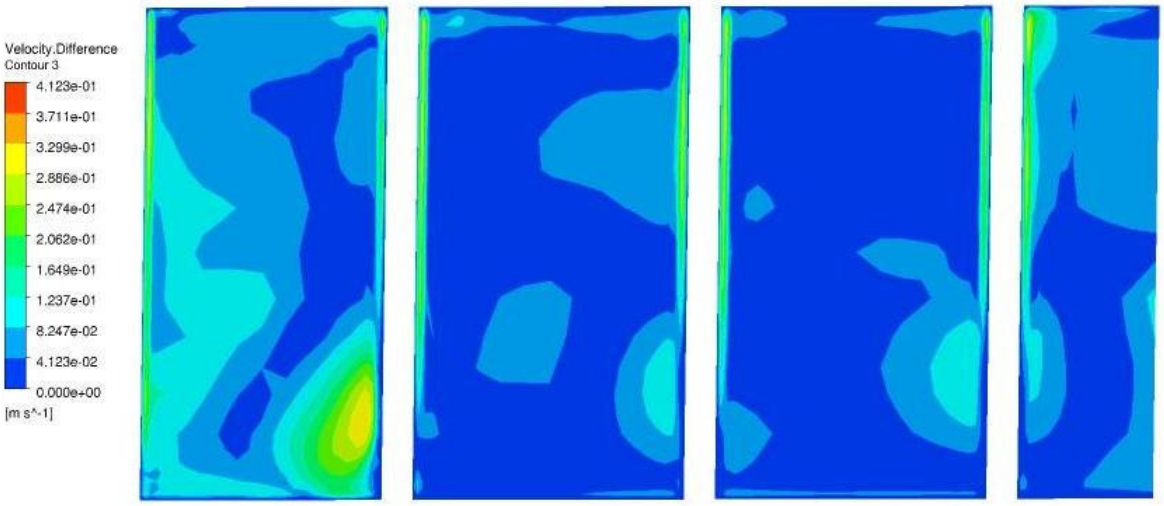

Figure 4.2. The differences in velocity for the intermediate mesh and the fine mesh. There is a symmetry plane in the middle of the fourth canal (right end).

As can be seen in Figs. 4.1 and 4.2 the difference in velocity is much larger in Fig. 4.1. In Fig. 4.2 the differences are slightly larger in canal 1 than in the other canals and this could explain why the mass flow rate differed the most there. However, the differences between the base case and the fine mesh were considered to be small, and thus the intermediate mesh was used in the rest of the simulations.

4.1.2. Varying the Mass Flow Rate

As presented in Section 3.2.3., three different mass flow rates were simulated. Table 4.3 summarises the results of the simulations. All velocities in this section have been normalised with the velocity in canals 1 and 7 in the 100% case.

Table 4.3. The normalised average velocity and the mass flow distribution of the seven canals, as well as the pressure drop over the cooling pass for the three different mass flow rates.

	50%	100%	150%
$\bar{v}_{1,7}$ [-]	0.5076	1	1.291
$\bar{v}_{2,6}$ [-]	0.5784	1.139	1.391
$\bar{v}_{3,5}$ [-]	0.6121	1.211	1.485
$\bar{v}_{4}$ [-]	0.6183	1.251	1.523
$\frac{\dot{m}_{1,7}}{\dot{m}_{tot}}$ [-]	0.1153	0.1150	0.1152
$\frac{\dot{m}_{2,6}}{\dot{m}_{tot}}$ [-]	0.1473	0.1476	0.1472
$\frac{\dot{m}_{3,5}}{\dot{m}_{tot}}$ [-]	0.1570	0.1570	0.1573
$\frac{\dot{m}_{4}}{\dot{m}_{tot}}$ [-]	0.1607	0.1609	0.1605
ΔP [Pa]	2.496	9.488	19.51

The velocity magnitude in the seven canals for 100% of the given mass flow can be seen in Figs. 4.3 and 4.4.

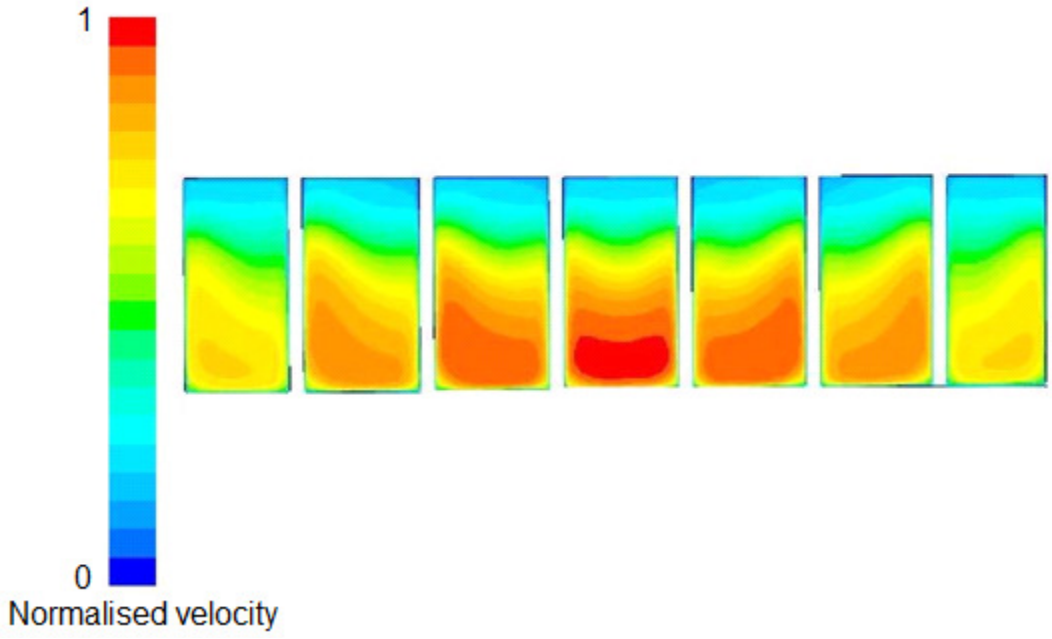

Figure 4.3. The velocity magnitude for a cross section of the cooling pass seen from above for the case with 100% of the mass flow rate.

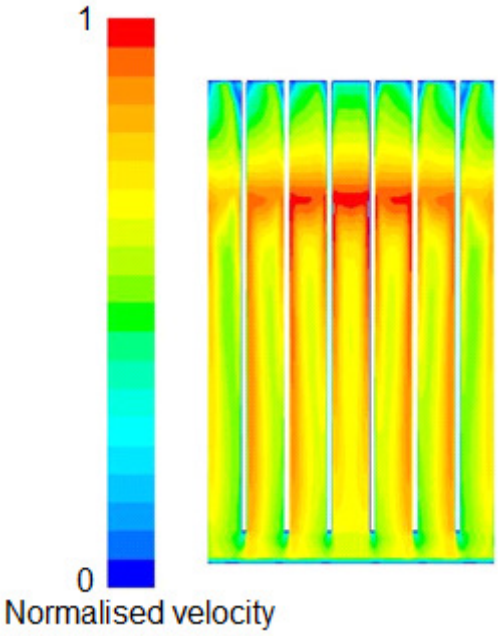

Figure 4.4. The velocity magnitude for a cross section of the cooling pass seen from the side for the case with 100 % of the mass flow rate.

As can be seen both in Table 4.3 and in Figs. 4.3 and 4.4, the canal in the middle (canal 4) had the largest velocity magnitude in most locations of the cooling pass. The velocity then decreased away from the centre and it was the lowest in canals 1 and 7. Since the cross sectional area and the density were assumed constant for canals 2-6, the differences of the mass flow rate depend only on the velocity and it was thus the highest for canal 4. The cross sectional area of canals 1 and 7 was slightly smaller than for the other canals and this explains the significantly lower mass flow rate in these canals.

From the results presented in Table 4.3, it is possible to conclude that the mass flow rate does not significantly affect the mass flow distribution between canals. The variations between runs are very small and they do not seem to follow a general trend.

4.1.3. Varying the Total Depth of the Cooling Pass

As presented in Section 3.2.3., simulations were carried out for three different total depths of the cooling pass. The results from these simulations can be seen in Table 4.4.

Table 4.4. The normalised average velocity, the mass flow distribution and the pressure loss over the cooling pass when decreasing or increasing the depth of all canals. The base case is also shown for comparison.

	50% of all depths	100% of all depths (base case)	150% of all depths
$\bar{v}_{1,7}$ [-]	2.006	1	0.7106
$\bar{v}_{2,6}$ [-]	2.150	1.139	0.8076
$\bar{v}_{3,5}$ [-]	2.243	1.211	0.8493
$\bar{v}_4$ [-]	2.310	1.251	0.8456
$\frac{\dot{m}_{1,7}}{\dot{m}_{tot}}$ [-]	0.1208	0.1150	0.1130
$\frac{\dot{m}_{2,6}}{\dot{m}_{tot}}$ [-]	0.1468	0.1476	0.1478
$\frac{\dot{m}_{3,5}}{\dot{m}_{tot}}$ [-]	0.1541	0.1570	0.1582
$\frac{\dot{m}_4}{\dot{m}_{tot}}$ [-]	0.1566	0.1609	0.1620
ΔP [Pa]	39.57	9.488	4.221

Table 4.4 shows that the flow gets more evenly distributed when the total depth of the cooling pass decreases. However, the differences are rather small, so it can be concluded that the total depth of the cooling pass does not significantly influence the mass flow distribution.

One remarkable observation is that the simulated average velocity in canal 4 for the case with the largest total depth is less than the average velocity in canals 3 and 5. This can be explained by the fact that the average velocity varies greatly along the canals and can thus at certain locations be less for canal 4 than for canal 3 and 5, see Fig. 4.5.

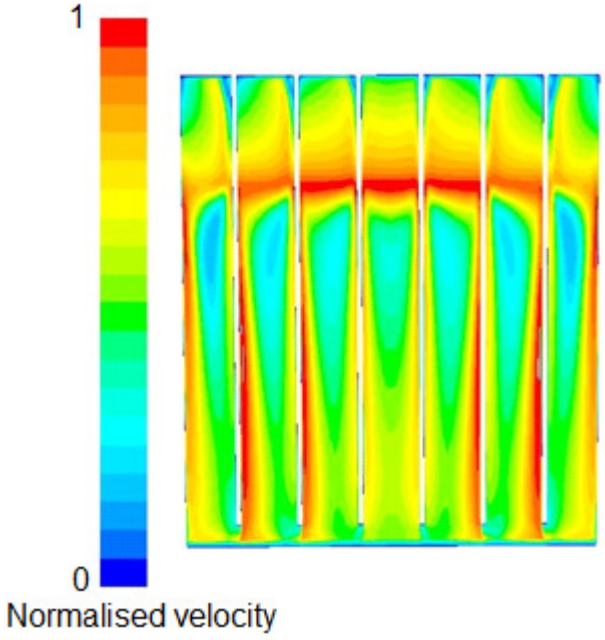

Figure 4.5. The velocity magnitude for a cross section of the cooling pass seen from the side for the case with the largest depth.

Figure 4.5 shows that there are indeed locations where the velocity appears to be larger in canals 3 and 5, but overall the velocity is larger in canal 4, explaining the larger mass flow rate in this canal.

4.1.4. Varying the Size of Canal 1 and 4 (for the Base Case Geometry)

The results from the simulations with varied canal size described in Section 3.2.3. can be seen in Table 4.5.

Table 4.5. The normalised average velocity, the mass flow distribution and the pressure loss over the cooling pass when varying the size of canal 1 or 4.

	50% of depth of canal 1	200% of depth of canal 1	50% of depth of canal 4	200% of depth of canal 4
$\bar{v}_{1,7}$ [-]	1.049	0.9175	1.078	0.8783
$\bar{v}_{2,6}$ [-]	1.285	0.9295	1.230	0.9636
$\bar{v}_{3,5}$ [-]	1.367	0.9888	1.333	0.9867
$\bar{v}_{4}$ [-]	1.413	1.012	1.293	1.025
$\frac{\dot{m}_{1,7}}{\dot{m}_{tot}}$ [-]	0.06089	0.1879	0.1248	0.1064
$\frac{\dot{m}_{2,6}}{\dot{m}_{tot}}$ [-]	0.1680	0.1203	0.1596	0.1288
$\frac{\dot{m}_{3,5}}{\dot{m}_{tot}}$ [-]	0.1792	0.1271	0.1727	0.1320
$\frac{\dot{m}_{4}}{\dot{m}_{tot}}$ [-]	0.1840	0.1294	0.08574	0.2657
ΔP [Pa]	12.32	6.135	11.53	6.484

As could be expected, canal 1 had a lower mass flow when its depth was decreased and a higher mass flow when its depth was decreased. The same is true for canal 4.

4.1.5. Varying the Number of Superheater Screens

The results from the simulations with 4 and 5 superheater screens described in Section 3.2.3. are presented in Tables 4.6 and 4.7, respectively.

Table 4.6. The mass flow distribution and the normalised average velocity in each canal, for the case with 4 superheater screens.

	$\frac{\dot{m}_{canal}}{\dot{m}_{tot}}$ [-]	Average normalised velocity [-]
Canal 1&5	0.1710	1.485
Canal 2&4	0.2168	1.676
Canal 3	0.2244	1.750

Table 4.7. The mass flow distribution and the normalised average velocity in each canal, for the case with 5 superheater screens.

	$\frac{\dot{m}_{canal}}{\dot{m}_{tot}}$ [-]	Average normalised velocity [-]
Canal 1&6	0.1381	1.203
Canal 2&5	0.1761	1.359
Canal 3&4	0.1858	1.435

The pressure losses for the different number of superheaters are presented in Table 4.8.

Table 4.8. Pressure loss over the cooling pass for 4, 5 and 6 superheater screens.

Number of screens	Pressure loss [Pa]
4	18.99
5	12.82
6	9.488

4.1.6. Correlation for the Mass Flow Distribution

As stated above, it could be concluded that the total mass flow rate and the total depth of the cooling pass did not significantly affect the mass flow distribution between canals. This implied that the mass flow distribution only depended on the velocity profile and the size of the canals. The velocities were the lowest in the canals closest to the edges and the highest in the canal in the centre of the cooling pass. The velocity profile varied with the total depth of the cooling pass: velocities were higher for smaller depths and vice versa.

Having this, the guess was that the mass flow distribution *only* depended the size and the position of the flue gas canals, and that factors such as the number of screens and the ratio between the sizes of two canals were irrelevant. This guess was investigated by plotting the relative depths of the canals against the total mass flow distribution at these points. The relative depth is defined as the distance from the edge to the point considered, divided by the total depth, see Fig. 4.6. According to Fig. 4.6, the total mass flow distribution is found by summation of the mass flow distribution to the left of the point considered. For example, if Fig. 4.6 is considered, the total mass flow distribution at point 1 is 11.5% and at point 2 it is 11.5%+14.76%=26.26%. Obviously, at point 7, the total mass flow distribution and the relative depth are equal to 1.

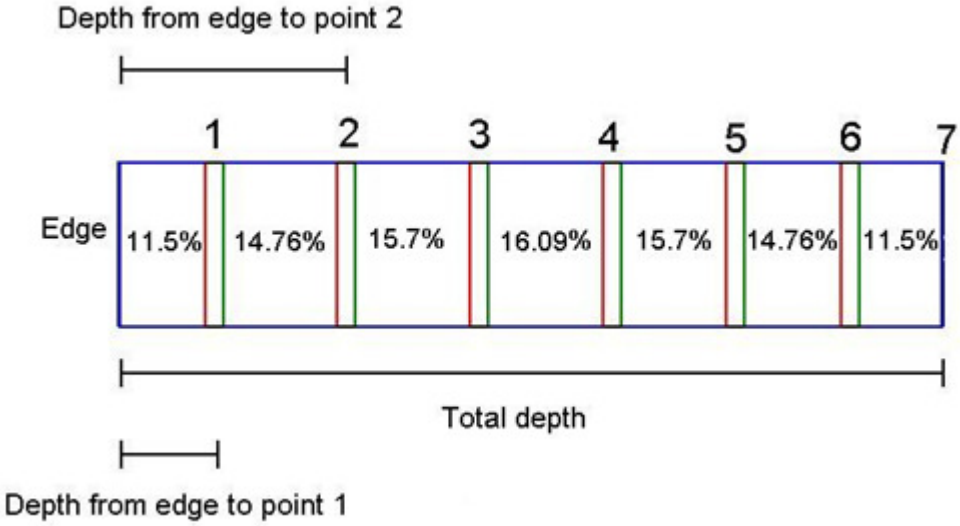

Figure 4.6. An example of the mass flow distribution and relative depths at seven different points. The figure is not to scale.

The total mass flow distribution and the relative depth at each point were determined for all the cases considered above and the result can be seen in Fig. 4.7.

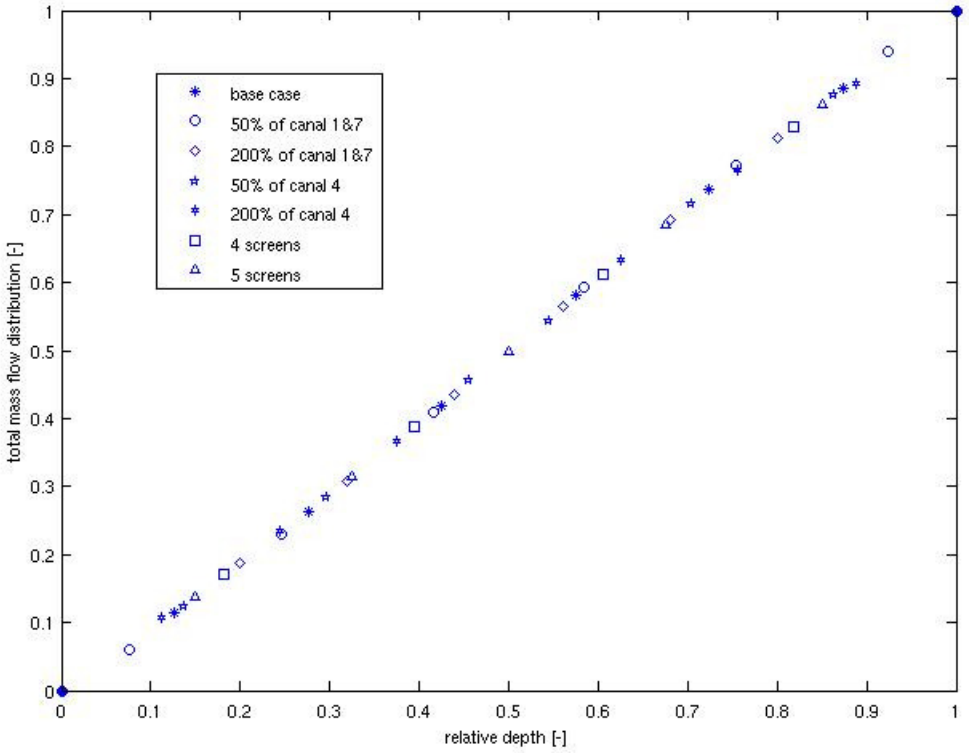

Figure 4.7. The total mass flow distribution as a function of the relative depth, for the base case, the cases with a varied canal depth and the cases with 4 and 5 screens.

Figure 4.7 shows that the number of screens and the ratio of the canal depths do not influence the mass flow distribution, they follow the same curve as the base case. A polynomial (Eq. 4.2) was created to fit the data points shown, see Fig. 4.8.

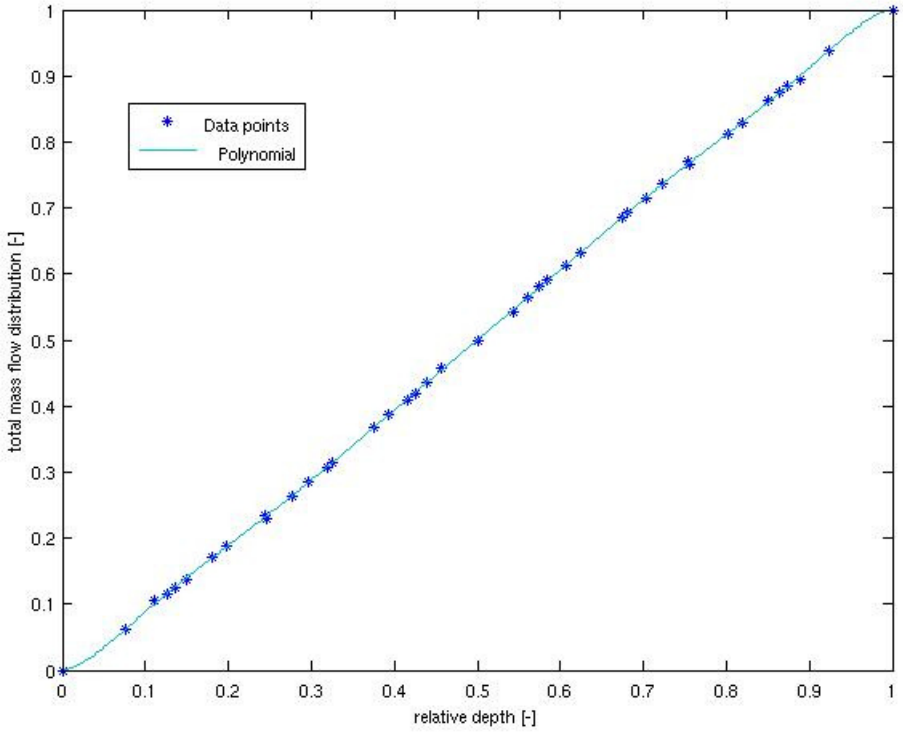

Figure 4.8. The data points in Fig. 4.7 fitted with a polynomial.

$$\frac{\dot{m}_{x-edge}}{\dot{m}_{tot}} = -330285x^9 + 1487.8x^8 - 2815.6x^7 + 2914.8x^6 - 1794.2x^5 + 667.06x^4 - 144.93x^3 + 16.867x^2 + 0.13212x - 6.6824 \times 10^{-5} \quad (4.2)$$

Equation 4.2. represents the normalised lateral distribution of the mass flow and can be used to find the mass flow distribution for each canal in the 1D model. For instance, the mass flow distribution at point 5 in Fig. 4.6 is calculated according to:

$$\frac{\dot{m}_5}{\dot{m}_{tot}} = \frac{\dot{m}_{5-edge}}{\dot{m}_{tot}} - \frac{\dot{m}_{4-edge}}{\dot{m}_{tot}} \quad (4.3)$$

4.1.7. Correlation for the Pressure Loss Over the Cooling Pass

The pressure loss of the flue gas for the different cases is presented in Tables 4.4 to 4.8: it is higher for higher mass flows, and higher for smaller depths of the cooling pass, which implies that it depends on the velocity of the flue gas. The average velocity of the flue gas entering the cooling pass was calculated according to:

$$v_{fg} = \frac{\dot{m}_{fg,tot}}{\rho_{fg} A_{cr,tot}} \quad (4.4)$$

Here the density is the average flue gas density in the cooling pass. The pressure loss for all different cases was plotted against the average velocity and the results can be seen in Fig. 4.9.

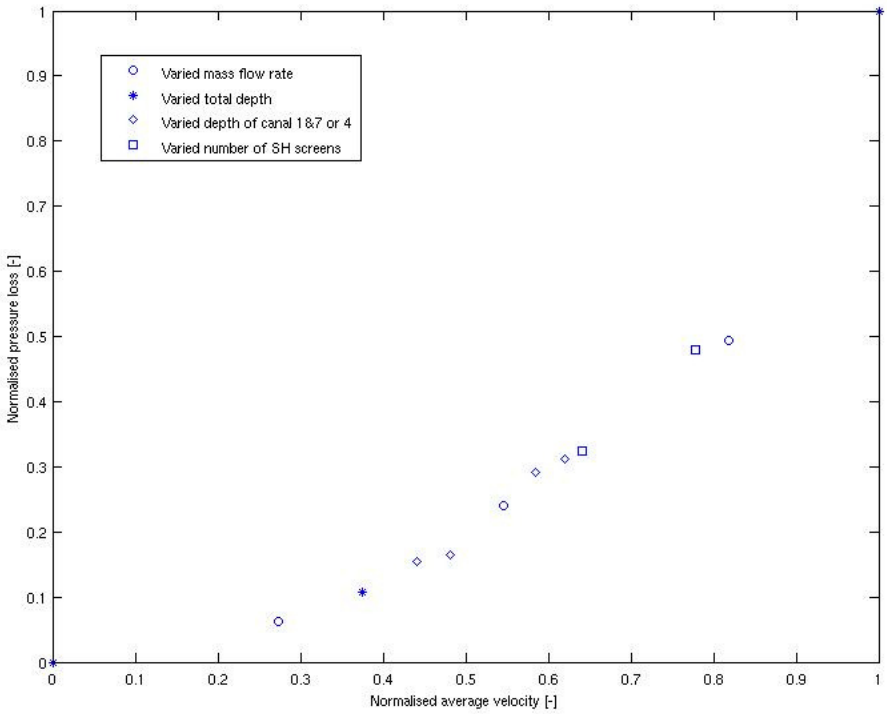

Figure 4.9. The normalised pressure drop as a function of the normalised average velocity of the cooling pass for the different cases.

Based on minimising the error rather than on attaining theoretical constraints, a 2nd grade polynomial (Eq. 4.5) was found to fit the values given in Fig. 4.9 (see Fig. 4.10):

$$\Delta P = 0.31348v^2 - 0.90406v + 1.0717 \quad (4.5)$$

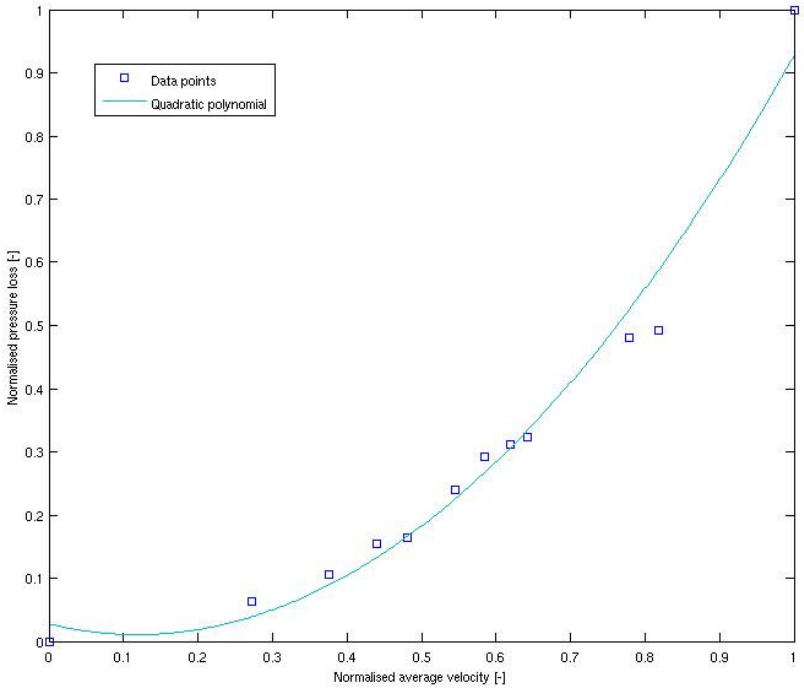

Figure 4.10. The data points in Fig. 4.9 fitted with a polynomial.

The proposed polynomial does not provide a consistent description of the pressure drop at very low velocities, but this is accepted since actual operational average velocity is never expected to be that low.

4.2. 1D Model

The four different routines created (one main function and three subfunctions) are described below.

The following input data represent inputs to the model and are therefore supplied in an Excel spreadsheet:

- flue gas inlet temperature
- water tube wall temperature
- inner steam inlet temperature
- absolute pressure of the steam
- flue gas composition
- number of superheater screens
- number of tubes per superheater screen
- height and width of the cooling pass
- depths of the different canals
- thermal conductivities for the ceramic, the steel in the water tube walls and the steel in the superheater screens
- the amount of metal studs per square meter
- the thicknesses of the superheater screens, water tube walls,
- the inner and outer diameters of the steam tubes
- the fouling coefficients for the water tube walls and the superheater screen surfaces

The main function calculates the flue gas and steam temperatures according to Section 2.5. and a new outlet steam temperature is guessed until convergence is reached. The program also calculates the pressure drop of the flue gas, the pressure drop of the steam and the fraction of the superheater screens that has a temperature above 650°C. The results are finally retrieved by the Excel spreadsheet.

The program fg_prop calculates flue gas properties (heat capacity, viscosity and thermal conductivity) as functions of the temperature and composition. The flue gas is assumed to consist of nitrogen, oxygen, carbon dioxide and water vapour. fg_emissivity calculates the flue gas emissivity as a function of the flue gas temperature, the mean beam length and the partial pressures of carbon dioxide and water vapour. Finally, view_factor calculates all the necessary view factors for the calculations, as a function of the number of cells, the width, the depth of each canal and the height of the cooling pass.

4.3. Validation of the 1D Model

A CFD simulation run with the DO-radiation model was used to validate the 1D model. With a case depicting heat transfer in the base case geometry, the incident radiation on the superheater screens and the flue gas outlet temperature obtained by the 1D model and the CFD simulations were compared. Since the CFD model did not include the steam inside the superheater screens, this temperature could not be examined. Figure 4.11 shows the incident radiation on the left side of superheater screens 1 and 2 (left and

right according to Fig 2.3). The incident radiation on these screens obtained by the 1D model is shown in Fig. 4.12. The results from the 1D model agreed fairly well with data obtained from the CFD run.

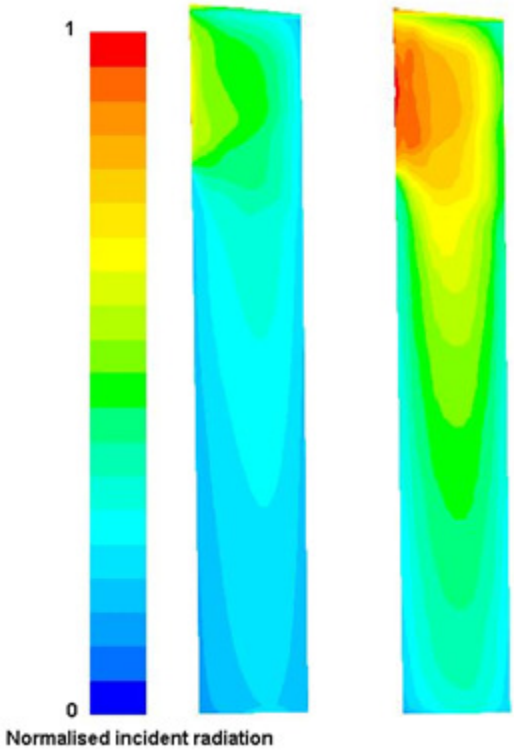

Figure 4.11. The normalised incident radiation on the left side of superheater screen 1 (to the left) and superheater screen 2 (to the right), obtained in the CFD-simulation.

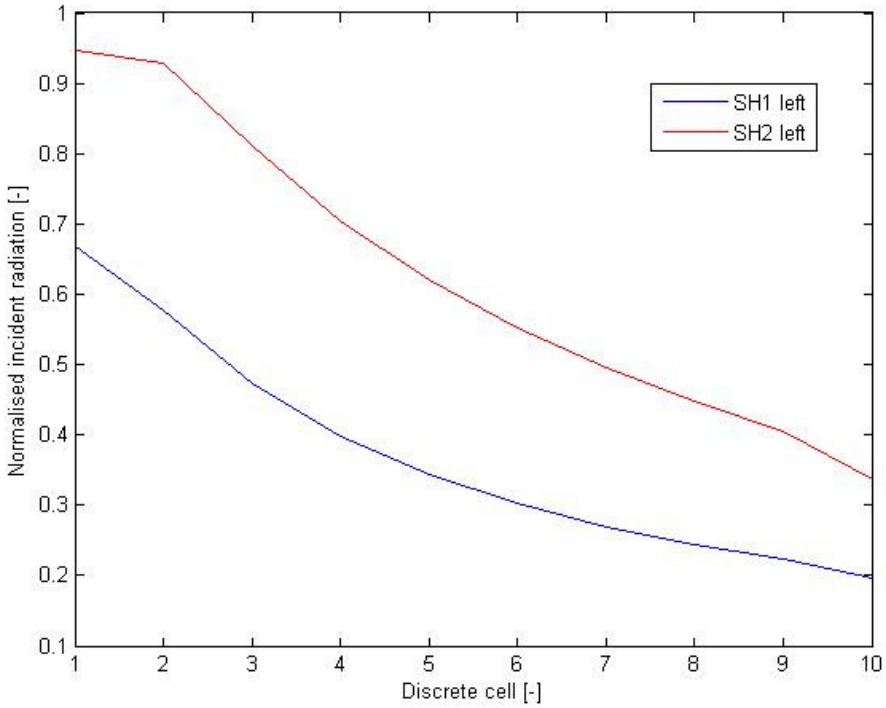

Figure 4.12. The normalised incident radiation per cell on the left side of superheater screens 1 and 2, obtained by the 1D model. Cell 1 is at the top and cell 10 is at the bottom of the cooling pass.

In both cases, the incident radiation was higher for screen 2 than screen 1, and the incident radiation decreased from the top to the bottom of the cooling pass. Figure 4.11 shows that the incident radiation varied across the screens, with higher values on the left side, where the flue gas entered the cooling pass.

The 1D model seems to overestimate the incident radiation at the top of the cooling pass, but in the second half of the cooling pass the two models agree better. A direct comparison at three different heights is given in Table 4.9.

Table 4.9. Incident radiation at three points, both for the 1D model and the CFD simulation. The incident radiation from the CFD simulation is area averaged.

	Screen 1 (1D)	Screen 1 (CFD)	Screen 2 (1D)	Screen 2 (CFD)
Top	0.6684	0.4875	0.9479	0.8125
Middle	0.3227	0.3125	0.5858	0.5250
Bottom	0.1974	0.2000	0.3370	0.3250

The normalised flue gas temperature profile from the CFD simulation can be seen in Fig. 4.13.

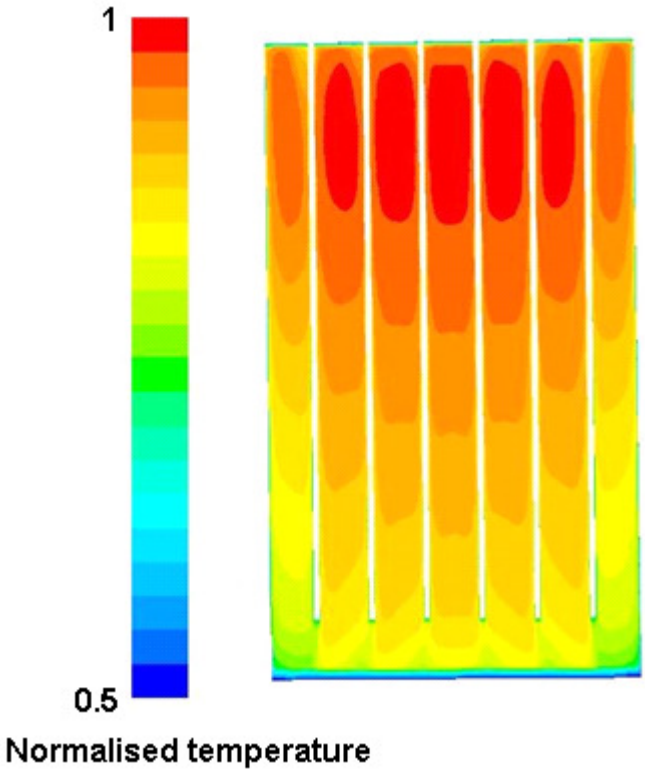

Figure 4.13. The normalised temperature profile of the different canals, obtained in the CFD-simulations.

Figure 4.14 shows the temperatures in the different canals obtained by the 1D model.

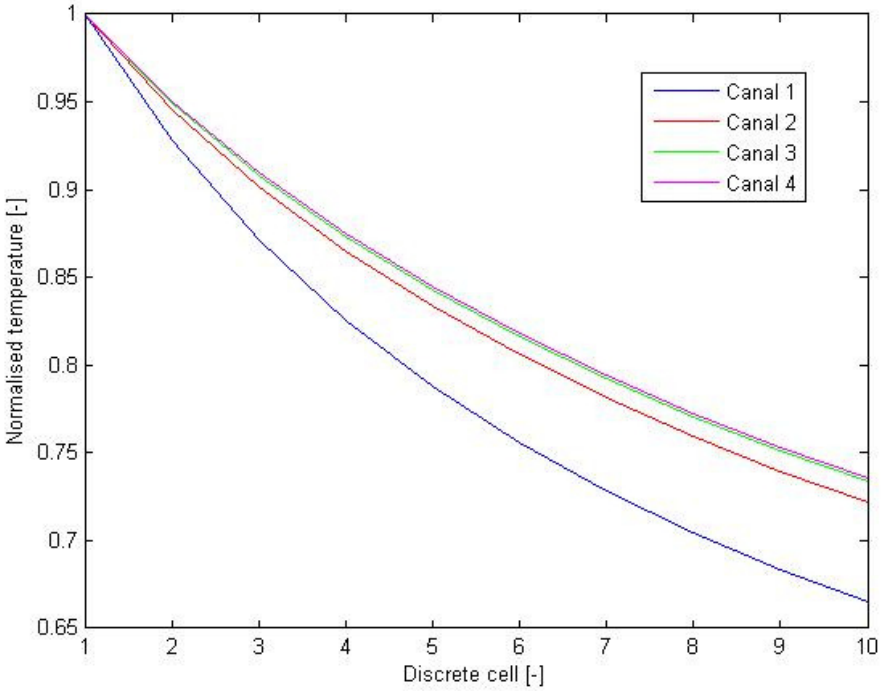

Figure 4.14. The normalised temperature per cell in each canal in the 1D model. Cell 1 is at the top of the cooling pass and cell 10 is at the bottom.

In both Fig. 4.13 and 4.14, the temperature is the highest in canal 4, and it is significantly lower in canal 1. This is due to the larger area of water tube walls in canal 1. The temperature does seem to decrease more quickly in the 1D model and at the outlet the two models differ with approximately 4.5% (calculated as the difference between the outlet temperature of the CFD simulation and the 1D model, divided by the difference between the inlet temperature and the outlet temperature of the CFD simulation).

4.4. Mesh-Dependency and Sensitivity Analysis of the 1D Model

The number of discrete cells in the 1D model was varied between 2 and 10 and the results can be seen in Fig. 4.15.

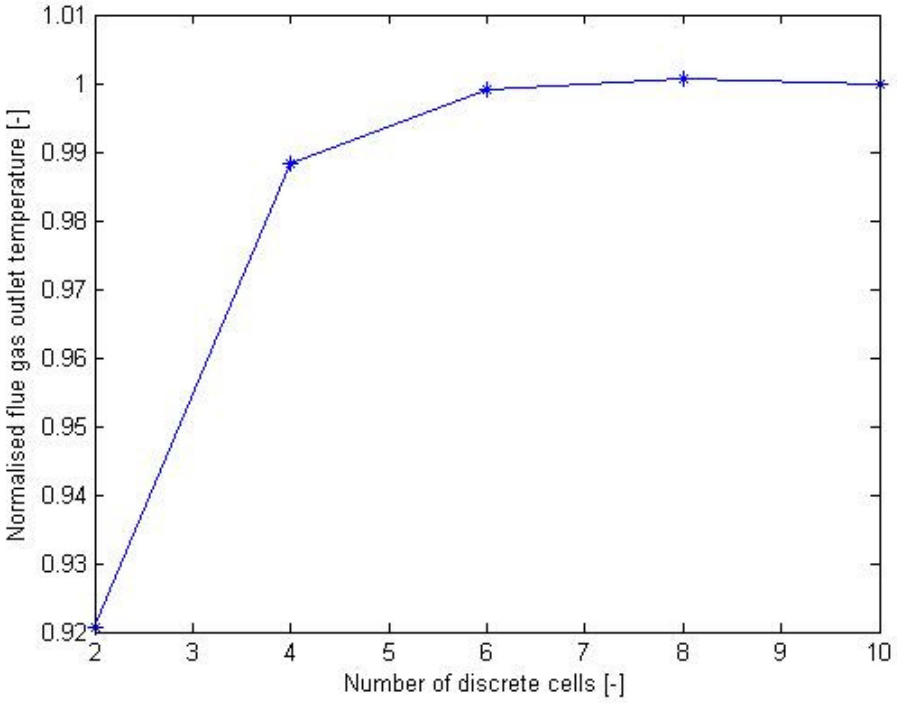

Figure 4.15. The normalised flue gas outlet temperature as a function of the number of discrete cells in the 1D model.

As can be seen in Fig. 4.15, it was sufficient to use eight or even six cells to get a solution that did not depend strongly on the number of cells. It is desirable to use as few cells as possible since the computational time needed for the simulation increases exponentially with each additional cell.

Treating the inlet and outlet as water tube walls ought to cause the flue gas to be cooled more than it should be. The flue gas radiation to the ceiling and floor of the 1D model was therefore excluded, and the surface emissivities were set to zero. These areas were also excluded when calculating the heat transfer through convection. This caused the flue gas outlet temperature to increase with approximately 5K.

Given the uncertainty of some input parameters in the 1D model, a sensitivity analysis was carried out. The wall emissivity of the superheater screens and the water tube walls and the convective heat transfer coefficient of the flue gas were studied. The results are

presented in Tables 4.10 and 4.11. The temperatures in the two tables have been normalised with the same flue gas temperature, based on a wall emissivity of 0.95 and the unchanged convective heat transfer coefficient, h_{fg}.

Table 4.10. The normalised flue gas outlet temperature when varying the wall emissivities.

Wall emissivity [-]	Normalised flue gas outlet temperature [-]
1	0.995
0.95	1
0.9	1.006
0.65	1.044

The flue gas outlet temperature changed somewhat when the wall emissivity was varied between 1 and 0.9, but the differences were not large. However, when decreasing the wall emissivity to 0.65, the flue gas temperature increased significantly, indicating that the wall emissivity should be chosen with care.

Table 4.11. The normalised flue gas outlet temperature when varying the convective heat transfer coefficient of the flue gas.

Convective heat transfer coefficient of the flue gas	Normalised flue gas outlet temperature [-]
$0.5h_{fg}$	1.016
h_{fg}	1
$2h_{fg}$	0.972

As can be seen in Table 4.11, the convective heat transfer coefficient of the flue gas notably affects the flue gas outlet temperature. When it is decreased the flue gas temperature increases and when it is increased the flue gas outlet temperature decreases, as could be expected.

5. Conclusions

- The field of CFD simulations on power boilers is growing and there are several articles written about CFD simulations on EfW-boilers and FBCs.
- The mass flow distribution and the pressure loss over the cooling pass do not depend on factors such as the mass flow rate and the number of screens. It is sufficient to calculate the relative depths of the canals to get the mass flow distribution. The pressure loss can be found by using a function of the average total velocity entering the cooling pass.
- For the flow field simulations, the mesh needed to be built of approximately half a million cells. The simulations based on this mesh took just over an hour to converge. The computational cost was decreased by using a symmetry plane in the middle of the cooling past, so that only half of the geometry needed to be modelled.
- The 1D model agreed fairly well with the CFD simulation with DO modelling of radiation, especially in the lower part of the cooling pass. The flue gas outlet temperature was 4.5% lower in the 1D model than in the CFD simulation.
- In the 1D model, the geometry could be modelled as rectangular canals, neglecting the inclination of the ceiling. The inlet and the outlet of the cooling pass could be treated as water tube walls.

References

[1] Bøjer, M., Jensen, .P. A., Frandsen, F., Dam-Johansen, K., Madsen, O. H., Lundtorp, K. (2008) Alkali/Chloride release during refuse incineration on a grate: Full-scale experimental findings. *Fuel Processing Technology*, vol. 89, nr 5, pp. 528-539.

[2] Lee, S-H., Themelis, N. J., Castaldi, M. J. (2007) High-Temperature Corrosion in Waste-to-Energy Boilers. *Journal of Thermal Spray Technology*, vol 16, nr 1, pp. 1-7.

[3] Ravelli S., Perdichizzi A., Barigozzi G. (2008) Description, applications and numerical modelling of bubbling fluidized bed combustion in waste-to-energy plants. *Progress in Energy and Combustion Science*, vol 34 (2), pp. 224-253.

[4] Kovács, J. (2001) What are the main characteristics of fluidized bed combustors? *IFRF Combustion Handbook.* http://www.handbook.ifrf.net/handbook/cf.html?id=87 (6 May 2012)

[5] Andersson B., Andersson R., Håkansson L., Mortensen M., Sudiyo R., van Wachem B. (2011) *Computational Fluid Dynamics for Chemical Engineers*. Gothenburg, March 2011.

[6] ANSYS FLUENT Theory Guide. (2010) U.S.A: SAS IP, inc.

[7] Balluch, M. (1995) Anisotropic scattering of light in the spherical geometry of the Earth's atmosphere. *Cambridge University, Centre for Atmospheric Science.* http://www.atm.damtp.cam.ac.uk/people/mgb/aniso.html (24 Jan. 2012)

[8] Patil, M.P., Sonolikrar, R.L. (2010) An approach for modeling thermal destruction of hazardous wastes in circulating fluidized bed incinerator. *Journal of Environmental Science and Engineering,* vol 50(4), pp. 289-298.

[9] Shah, M. T., Utikar, R.P., Evans, G.M., Tade, M.O., Pareek, V.K. (2011) CFD simulations of gas-solid flows in a CFB riser: Effect of inlet boundary conditions. *International Congress on Modelling and Simulation*; 12-16 December 2011, Perth, Australia.

[10] Phongphiphat, A., Ryu, C., Yang, Y.B., Finney, K. N., Leyland, A., Sharifi, V. N., Swithenbank, J. (2010) Investigation into high-temperature corrosion in a large-scale municipal waste-to-energy plant. *Corrosion Science,* vol 52(12), pp. 3861-3874.

[11] Welty, J.R., Wicks, C.E., Wilson, R.E., Rorrer, G. (2001) *Fundamentals of Momentum, Heat, and Mass Transfer.* 4th edition. Hoboken, New Jersey: John Wiley & Sons, Inc.

[12] Larry W. Mays, L. W. (1999) *Hydraulic Design Handbook*, 1st edition. New York: McGraw-Hill Companies.

[13] Jones, B. (1997) Viscous Grid Spacing Calculator. *National Aeronautics and Space Administration*. http://geolab.larc.nasa.gov/APPS/YPlus/ (28 May 2012)

[14] McBride, B. J., Gordon, S., Reno, M.A. (1993) *Calculating Thermodynamic and Transport Properties of Individual Species.* [Electronic] National Aeronautics and Space Administration, Cleveland, Ohio.

[15] Idevo AB. (2010) Density of Flue Gases http://www.idevo.se (28 May 2012)

[16] Incropera, F.P., Dewitt, D.P., Lavine, A., Bergman T.L. (2007) *Fundamentals of Heat and Mass Transfer.* 6th edition. Hoboken, New Jersey: John Wiley & Sons, Inc.

[17] Verein Deutscher Ingenieure. (1984) *VDI Wärmeatlas.* 4th edition. Düsseldorf: VDI-Verlag Gmb H.

[18] Baskakov, A.P., Leckner, B. (1997) Radiative Heat Transfer in Circulating Fluidized Bed Furnaces. *Powder Technology*, vol 90(3), pp. 213-218.

Appendix A: Steam and Flue Gas Properties

Since the properties of the steam and the flue gases change with temperature and pressure, steam tables and polynomials were used in the calculations. The steam properties were obtained with the open source program XSteam, used as a function file in Scilab. The viscosity, the thermal conductivity and the specific heat of the outer and inner steam for each discrete step were obtained in this way.

For the flue gas, the pressure could be considered constant at 1 bar in the cooling pass, but the flue gas temperature decreased as the flue gas flowed down the cooling pass. Temperature dependant polynomials could be used to describe how the flue gas properties changed with temperature. These polynomials are described below along with some assumptions that were made in the calculations.

Since the flue gases were assumed to have a constant total pressure of 1 bar, it was possible to use NASA polynomials for the flue gas components [14]. The NASA polynomials can be used to evaluate the specific heats, the viscosities and the thermal conductivities for gases at standard conditions (1 bar). It was assumed that a linearisation of the properties of the flue gas components gave a sufficiently good result. The specific heat was thus calculated as:

$$C_{p,fg} = X_{N_2} C_{p,N_2} + X_{O_2} C_{p,O_2} + X_{H_2O} C_{p,H_2O} + X_{CO_2} C_{p,CO_2} \qquad (A1)$$

The flue gas viscosity and thermal conductivity were approximated in the same way.

The specific heats of the flue gas components were calculated with the polynomial in Eq. A2 [14]:

$$C_{p,i} = (a_{1,i} + a_{2,i} T_{fg} + a_{3,i} T_{fg}^2 + a_{4,i} T_{fg}^3 + a_{5,i} T_{fg}^4) \cdot \frac{R}{M_i} \left[\frac{J}{kgK}\right] \qquad (A2)$$

Here i represents the different flue gas components and $a_{1,2,3,4,5}$ are constants that can be found in Tables A1 and A2. R is the gas constant (8.31447J/mol/K) and M_i is the molar weight of component i. Two different temperature intervals were used for the constants: $T_{fg} < 1000K$ and $T_{fg} \geq 1000K$.

Table A1. Constants for the calculation of $C_{p,i}$ for $T_{fg} < 1000$ [14].

	a_1	a_2	a_3	a_4	a_5
N_2	3.53100528	-1.23660987×10^{-4}	-5.02999437×10^{-7}	2.43530612×10^{-9}	$-1.40881235\times10^{-12}$
O_2	3.78245636	-2.99673415×10^{-3}	9.847302×10^{-6}	-9.68129508×10^{-9}	3.24372836×10^{-12}
H_2O	4.19864056	-2.03643410×10^{-3}	6.52040211×10^{-6}	-5.48797062×10^{-9}	1.77197817×10^{-12}
CO_2	2.35677352	8.98459677×10^{-3}	-7.12356269×10^{-6}	2.45919022×10^{-9}	$-1.43699548\times10^{-13}$

Table A2. Constants for the calculation of $C_{p,i}$ for $T_{fg} \geq 1000K$ [14].

	a_1	a_2	a_3	a_4	a_5
N_2	2.95257626	1.39690057×10^{-3}	-4.92631691×10^{-7}	7.86010367×10^{-11}	$-4.60755321\times10^{-15}$
O_2	3.66096083	6.56365523×10^{-4}	-1.41149485×10^{-7}	2.05797658×10^{-11}	$-1.29913248\times10^{-15}$
H_2O	2.67703787	2.97318329×10^{-3}	-7.73769690×10^{-7}	9.44336689×10^{-11}	$-4.26900959\times10^{-15}$
CO_2	4.63659493	2.74131991×10^{-3}	-9.95828531×10^{-7}	1.60373011×10^{-10}	$-9.16103468\times10^{-15}$

Equation A3 was used to calculate the viscosities of the flue gas components [14].

$$\mu_i = \exp\left(A_i \cdot ln(T_{fg}) + \frac{B_i}{T_{fg}} + \frac{C_i}{T_{fg}^2} + D_i\right) \cdot 10^{-7}\ [Pas] \qquad (A3)$$

Here A_i, B_i, C_i and D_i are constants that can be found in Tables A3 and A4. Two different temperature intervals were used for the constants: $300 \leq T_{fg} \leq 1000K$ and $1000K < T_{fg} \leq 5000K$.

Table A3. Constants for the calculation of μ_i for $300 \leq T_{fg} \leq 1000K$ [14].

	A	B	C	D
N_2	0.60443938	-0.43632704×10^2	-0.88441949×10^3	1.8972150
O_2	0.61936357	-0.44608607×10^2	-0.13460714×10^4	1.9597562
H_2O	0.78387780	-0.38260408e×10^3	0.49040158×10^5	0.85222785
CO_2	0.54330318	-0.18823898×10^3	0.88726567×10^4	2.4499362

Table A4. Constants for the calculation of μ_i for $1000K < T_{fg} \leq 5000K$ [14].

	A	B	C	D
N_2	0.65060585	0.28517449×10^2	-0.16690236×10^5	1.5223271
O_2	0.63839563	-1.2344438	-0.2288581×10^5	1.8056937
H_2O	0.50714993	-0.68966913×10^3	0.87454750×10^5	3.0285155
CO_2	0.65318879	0.51738759×10^2	-0.62834882×10^5	1.5227045

The thermal conductivities of the flue gas components were evaluated in a similar way to the viscosities [14]:

$$\lambda_i = \exp\left(A_i \cdot ln(T_{fg}) + \frac{B_i}{T_{fg}} + \frac{C_i}{T_{fg}^2} + D_i\right) \cdot 10^{-4}\ \left[\frac{W}{mK}\right] \qquad (A4)$$

Here A_i, B_i, C_i and D_i are constants that can be found in Tables A5 and A6. Two different temperature intervals were used for the constants: $300 \leq T_{fg} \leq 1000K$ and $1000K < T_{fg} \leq 5000K$.

Table A5. Constants for the calculation of λ_i for $300 \leq T_{fg} \leq 1000K$ [14].

	A	B	C	D
N_2	0.94306384	0.12279898×10^3	-0.11839435×10^5	-0.10668773
O_2	0.81595343	-0.34366856×10^3	0.22785080×10^4	1.0050999
H_2O	1.5541443	0.66106305×10^2	0.55969886×10^4	-3.9259598
CO_2	0.53726173	-0.49928331×10^3	0.37397504×10^5	3.2903619

Table A6. Constants for the calculation of λ_i for $1000K < T_{fg} \leq 5000K$ [14].

	A	B	C	D
N_2	0.65147781	-0.15059801×10^{3}	-0.1374676×10^{5}	2.1801632
O_2	0.80805788	0.11982181×10^{3}	-0.47335931×10^{5}	0.95189193
H_2O	0.79349503	-0.13340063×10^{4}	0.37864327×10^{6}	2.3591474
CO_2	0.66068182	-0.12741845×10^{3}	-0.81580328×10^{5}	2.1817907

The density of the flue gas varies with pressure and temperature. If the pressure can be assumed to be fairly constant, Eq. A5 can be used to approximate the total density [15].

$$\rho_{fg} = \left(X_{N_2}\rho_{0,N_2} + X_{O_2}\rho_{0,O_2} + X_{H_2O}\rho_{0,H_2O} + X_{CO_2}\rho_{0,CO_2}\right)\frac{273}{T_{fg} + 273} \qquad (A5)$$

Here 0 stands for standard conditions (1 bar and 0°C). The density at standard conditions for the flue gas components can be found in Table A7.

Table A7. Densities at standard conditions for the flue gas components [15].

I	$\rho_{o,i}$ [kg/m^3]
N_2	1.25
O_2	1.43
H_2O	0.804
CO_2	1.977

Appendix B: View Factor

The different view factors could all be found analytically since the geometry was fairly simple. View factors for opposing faces and perpendicular faces with a common edge were needed. They can be described with Eqs. B1 and B2 respectively [16].

$$F_{ij} = \frac{2}{\pi \bar{X}\bar{Y}}\left\{ln\left(\left[\frac{(1+\bar{X}^2)(1+\bar{Y}^2)}{1+\bar{X}^2+\bar{Y}^2}\right]^{0.5}\right) + \bar{X}(1+\bar{Y}^2)^{0.5}tan^{-1}\frac{\bar{X}}{(1+\bar{Y}^2)^{0.5}} + \bar{Y}(1+\bar{X}^2)^{0.5}tan^{-1}\frac{\bar{Y}}{(1+\bar{X}^2)^{0.5}} - \bar{X}tan^{-1}\bar{X} - \bar{Y}tan^{-1}\bar{Y}\right\} \quad (B1)$$

$\bar{X} = X/L$ and $\bar{Y} = Y/L$ where X and Y are the sides of the faces and L is the distance between the faces.

$$F_{ij} = \frac{1}{\pi W}\left(Wtan^{-1}\frac{1}{W} + Htan^{-1}\frac{1}{H} - (H^2+W^2)^{0.5}tan^{-1}\frac{1}{(H^2+W^2)^{0.5}} + \frac{1}{4}ln\left\{\frac{(1+W^2)(1+H^2)}{1+W^2+H^2}\left[\frac{W^2(1+W^2+H^2)}{(1+W^2)(W^2+H^2)}\right]^{W^2} \times \left[\frac{H^2(1+H^2+W^2)}{(1+H^2)(H^2+W^2)}\right]^{H^2}\right\}\right) \quad (B2)$$

$H = Z/X$ and $W = Y/X$ where X is the common edge of faces i and j. Y and Z are the other edges of face i and j respectively.

It was also necessary to be able to calculate the view factor for the scenarios depicted in Figs. B1 and B2.

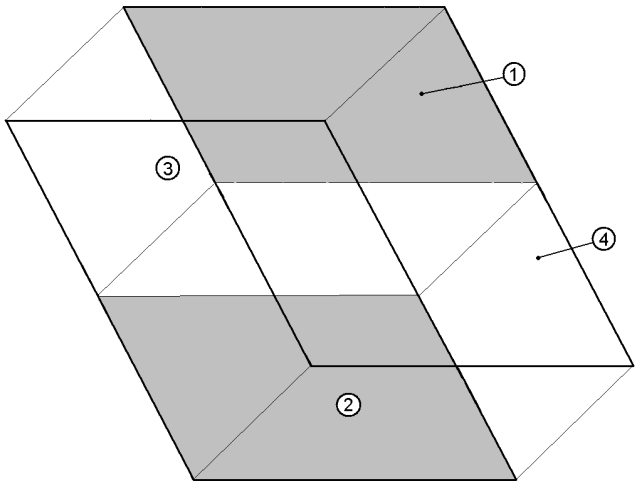

Figure B1. Scheme showing two faces that are not directly opposite of each other.

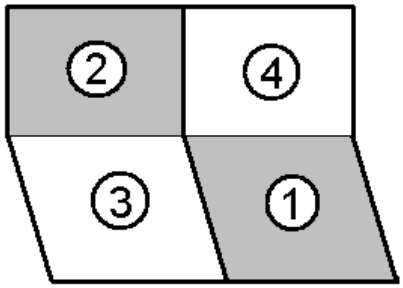

Figure B2. Scheme showing two perpendicular faces without a common edge.

For the geometry shown in Fig. B1, if $A_1 = A_2 = A_3 = A_4$, the view factor F_{12} is found with:

$$F_{12} = F_{(1,4)(2,3)} - F_{13} \qquad (B3)$$

where $F_{(1,4)(2,3)}$ is the view factor from the combined area of A_1 and A_4 to the combined area of A_2 and A_3.

For the geometry shown in Fig. B2, if $A_1 = A_3$ the view factor between area 1 and 2 is calculated as:

$$F_{12} = F_{(1,3)(2,4)} - F_{14} \qquad (B4)$$

Appendix C: Flue Gas Emissivity

In the model, the flue gas emissivity depended on factors such as the partial pressures of carbon dioxide and water vapour, the flue gas temperature and the mean beam length. It could be found by first finding the emissivities of water vapour and carbon dioxide. A correction factor was then needed to deal with the nonlinearity caused by the overlap in radiation spectra. The gas emissivity was calculated as: [17]

$$\varepsilon_{fg} = f_k\left(\varepsilon_{H_2O} + \varepsilon_{CO_2}\right) \quad (C1)$$

The water emissivity was found using Fig. 4 in VDI-Wärmeatlas (1984) [17]. The figure was converted to a 21×11 matrix with values of the water vapour emissivity for different mean beam lengths multiplied with the partial pressure of water vapour, for each row, and different temperatures for each column. Linear interpolation was then used to find the water emissivity for a specific temperature and a specific mean beam length. The temperatures ranged between 800K and 1300K, with a temperature increase of 50K between each column. The mean beam lengths multiplied with the partial pressure of water vapour that were used are given in Table C1.

Table C1. Values of the mean beam length times the partial pressure of water vapour used to generate the matrix described in the text.

$p_{H_2O} \times s$ [bar m]	0.06
6	0.05
3	0.04
1.5	0.03
1	0.025
0.6	0.020
0.5	0.018
0.4	0.015
0.3	0.012
0.25	0.010
0.20	0.009
0.15	0.007
0.12	0.006
0.10	0.005
0.07	0.004

The emissivity for carbon dioxide was calculated with Eqs. C2 to C4. The constants used in Eq. C2 can be found in Table C2 [17].

$$a_i = \frac{b_i(p_{CO_2}s)^{n_i}}{c_i + (p_{CO_2}s)^{n_i}} + \frac{(a_{\infty i} - b_i)(p_{CO_2}s)^{m_i}}{d_i + (p_{CO_2}s)^{m_i}} \quad (C2)$$

$$\gamma = \frac{1273 - T_{fg}}{1000} \quad (C3)$$

$$\varepsilon_{CO_2} = a_1 + a_2\gamma + a_3\gamma^2 + a_4\gamma^3 \quad (C4)$$

Table C2. Constants used for the calculation of the emissivity of carbon dioxide [17].

i	$a_{\infty i}$	b_i	c_i	d_i	m_i	n_i
1	0.252	0.1166	0.04	0.477	1.542	0.802
2	0.01	0.0658	0.0245	1.712	0.25	0.715
3	-0.0955	-0.0535	0.013	0.115	2.45	1.076
4	-0.0303	-0.0806	0.0816	0.691	0.13	0.495

The correction factor was calculated using Eqs. C5 to C7 [17].

$$\sum ps = sp_{H_2O} + sp_{CO_2} \tag{C5}$$

$$z = \frac{sp_{CO_2}}{\sum ps} \tag{C6}$$

$$f_k = 1 + \frac{0.25 \sum ps}{0.11 + \sum ps} (1 - z)\ln(1 - z) \tag{C7}$$

The dust or ash particles of the flue gases also contributed to emission and absorption. The emissivity of the particulate phase could be calculated as: [18]

$$\varepsilon_{part} = 1 - e^{\frac{-1.5 C_v \varepsilon_{part} s}{ds}} \tag{C8}$$

Here C_v is the volumetric fraction of dust particles. The particle emissivity, ε_{part}, was set to a constant value of 0.88. The total flue gas emissivity was found by summation of the gas emissivity and the particle emissivity.

The mean beam length is a measure of the average thickness of the gas through which a beam passes. It depends on the geometry and a few different mean beam lengths were calculated in the 1D model.

The mean beam length for gas-surface radiation within a cell was calculated with Eq. C9, where y represent the cell projected surfaces from which the beam is evaluated, see Fig. 2.4. The mean beam length for the gas-gas radiation was calculated in a similar way but with the gas area (represented by the top or bottom of the "gas box" see Fig. 2.4) in the denominator of Eq. C9.

$$s_{gy} = \frac{3.6V}{A_y} \tag{C9}$$

For the gas radiation to surfaces of neighbouring cells, "z-surfaces", the mean beam length was calculated with Eq. C10, which represents the distance between the centre of the gas surface to the centre of the neighbouring surface, see Fig. C1. This equation was also used when calculating the mean beam length for the gas absorption that occurred through this type of radiation (the last two terms in Eq. 2.34).

$$s_{gz} = \sqrt{(0.5d, w)^2 + (0.5\Delta x)^2} \tag{C10}$$

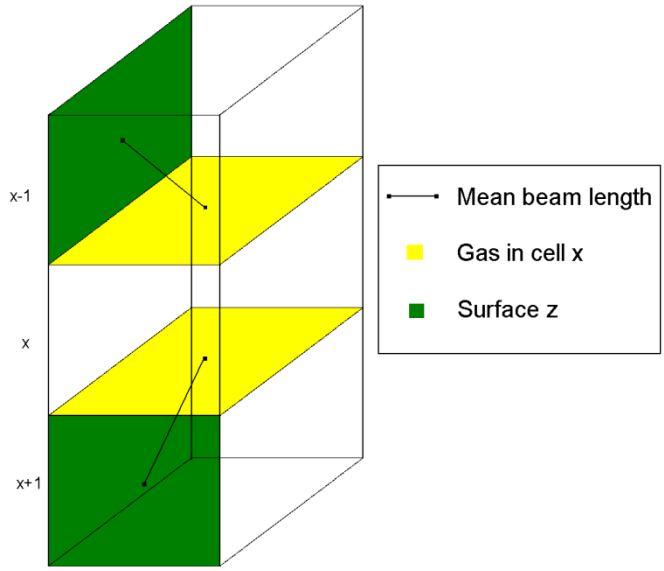

Fig. C1. Mean beam lengths from the gas in cell x to two arbitrary surfaces in the adjacent cells.

The gas absorption taking place during the surface-surface radiation also required a mean beam length. It was taken as the distance between the centre of a surface in step n to the centre of a surface in step m. It was calculated according to Eq. C11 for opposing surfaces and according to Eq. C12 for perpendicular surfaces, see Fig. C2.

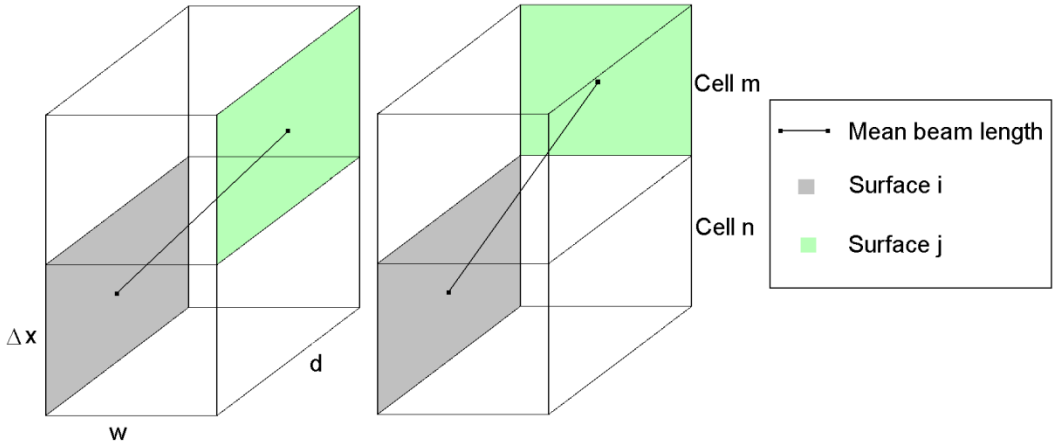

Figure C2. Mean beam length between opposing surfaces (to the left) and for perpendicular surfaces (to the right). Note that surface j can be in any cell, not just the adjacent cells.

$$s_{ji} = \sqrt{(d,w)^2 + (\Delta x(n-m))^2} \qquad (C11)$$

$$s_{ji} = \sqrt{(0.5d)^2 + (0.5w)^2 + (\Delta x(n-m))^2} \qquad (C12)$$

The temperature used when calculating the gas absorption between the different surfaces is taken as the average flue gas temperature of these cells, i.e.

$$\bar{T}_{nm} = \frac{T_n + T_m}{2} \qquad (C13)$$

As shown in Figs. 2.7 and 2.8, a certain part of the radiation of the surface-surface radiation and the gas-surface radiation was absorbed by the gas on the way. The gas absorption α was calculated with the same equations and mean beam lengths as the emissivity.

Equation 2.34 contains the factor $\varphi_{ji,x}$, which represents the fraction of radiative heat absorbed by the gas in cell x, when surface j radiates to surface i, see Fig. C3. It is assumed that the energy absorbed can be divided evenly between the cells, although the absorption decreases exponentially along the beam path. The absorption is also temperature dependent, and this is not taken into account. In the model, the cells where the beam originates from and is destined absorb half as much energy as the cells that the beam passes through completely, as shown in Eqs. C14 and C15, respectively. If the surfaces are located in the same cell ($m = n$), then $\varphi_{ji,x} = 1$.

$$\varphi_{ji,x} = \frac{1}{2(m-n)} \qquad (C14)$$

$$\varphi_{ji,x} = \frac{2}{2(m-n)} = \frac{1}{(m-n)} \qquad (C15)$$

If the case in Fig. C3 is considered, cell 1 and 3 would thus receive 25% of the absorbed radiation each, while cell 2 would receive 50%.

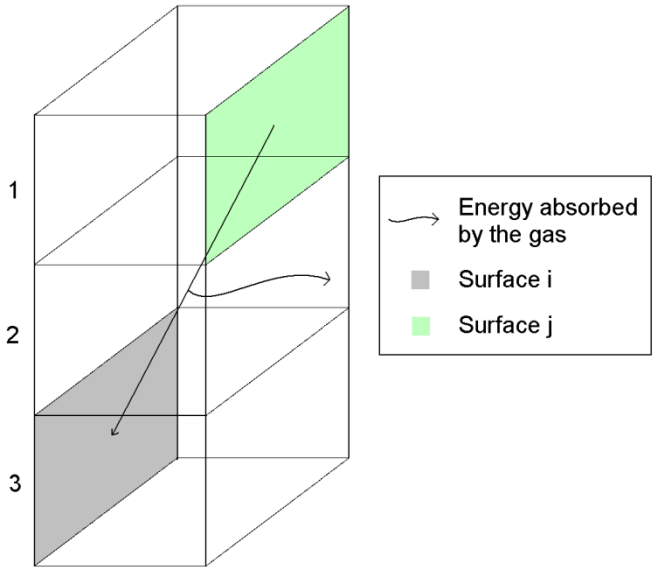

Figure C3. Surface j in cell 1 radiates to surface i in cell 3. Some of the radiative heat is absorbed by the gas and does not reach surface i.